Thermodynamically consistent modelling of two-phase flows with moving contact line and soluble surfactants

Thermodynamically consistent modelling of two-phase flows with moving contact line and soluble surfactants

Guangpu Zhu[a, +], Jisheng Kou[b, e, +], Bowen Yao[c], Yu-shu Wu[c], Jun Yao[a, *], Shuyu Sun [d, *]

[a]*Research Center of Multiphase Flow in Porous Media, School of Petroleum Engineering, China University of Petroleum (East China), Qingdao 266580, China.*
[b] *School of Civil Engineering, Shaoxing University, Shaoxing 312000, Zhejiang, China.*
[c]*Department of Petroleum Engineering, Colorado School of Mines, 1600 Arapahoe St., Golden, CO 80401, United States.*
[d]*Computational Transport Phenomena Laboratory, Division of Physical Science and Engineering, King Abdullah University of Science and Technology, Thuwal 23955-6900, Kingdom of Saudi Arabia.*
[e]*School of Mathematics and Statistics, Hubei Engineering University, Xiaogan 432000, Hubei, China.*
** corresponding authors*
+ G. Zhu and J. Kou contribute equally to this manuscript.
Contact information: b16020069@s.upc.edu.cn (G. Zhu), rcogfr_upc@126.com (J. Yao), shuyu.sun@kaust.edu.sa (S. Sun)

Abstract

Droplet dynamics on the solid substrate is significantly influenced by surfactants. It remains a challenge task to model and simulate the moving contact line dynamics with soluble surfactants. In this work, we present a derivation of the phase-field moving contact line model with soluble surfactants through the first law of thermodynamics, related thermodynamical relations and the Onsager's variational principle. The derived thermodynamically consistent model consists of two Cahn–Hilliard–type equations governing the evolution of interface and surfactant concentration, the incompressible Navier–Stokes equations and the generalized Navier boundary condition (GNBC) for the moving contact line. With chemical potentials derived from the free energy functional, we analytically obtain certain equilibrium properties of surfactant adsorption, including equilibrium profiles for phase-field variables, the Langmuir isotherm and the equilibrium equation of state. A classical droplet spread case is used to numerically validate the moving contact line model and equilibrium properties of surfactant adsorption. The influence of surfactants on the contact line dynamics observed in our simulations is consistent with the results obtained by sharp interface models. Using the proposed model, we investigate the droplet dynamics with soluble surfactants on a chemically patterned surface. It is observed that droplets will form three typical flow states as a result of different surfactant bulk concentrations and defect strengths, specifically, the coalescence mode, the non-coalescence mode and the detachment mode. In addition, a phase diagram for the three flow states is presented. Finally, we study the unbalanced Young stress acting on triple-phase contact points. The unbalanced Young stress could be a driving or resistance force, which is determined by the critical defect strength.

keywords: soluble surfactants; moving contact line; droplet dynamics; phase-field model

1. Introduction

The flow of droplets on a solid surface is ubiquitous in nature and many industrial applications, ranging from spray coating, crude oil recovery and microfluidics to ink jet printing (Dupuis & Yeomans 2005; Patil et al. 2016; Blake et al. 2015). The droplet dynamics is significantly dependent on the properties of a solid surface, e.g., the wettability (Blake et al. 2015; Shang et al. 2019). Surfactants, interface active agents, can change wetting properties of a solid surface by altering the

contact angle (Lai et al. 2010; Xu & Ren 2014; Zhang et al. 2014). An interesting example in our daily life is that we add detergents (surfactants) in a washing machine to clean clothes effectively. Oil droplets that stick to clothes becomes less "sticky" under the effect of surfactants, and the water currents can wash away droplets readily. Another typical example is the surfactant-based enhanced oil recovery in the petroleum industry. Adding surfactants into the injected water can greatly improve the efficiency of drainage, since oil droplets attached on the surface of hydrophobic rock are easier to be displaced away (Raffa et al. 2016). Surfactants and wettability of reservoir rocks determine the efficiency of drainage and the distribution of residual oil in porous media. In above examples, water, oil droplets, clothes (rock) and surfactants make up a typical multiphase system involving the moving contact line (MCL) and surfactants. Therefore, an interesting and practically important issue arises concerning how surfactants affect the dynamics of MCL.

Numerical modelling is taking an increasingly significant position in investigating the droplet dynamics on a solid surface with surfactants, as it can provide easier access to some quantities such as surfactant concentration, pressure and velocity, which are difficult to measure experimentally (Liu et al. 2018). However, the efficient and accurate computational modelling of contact line dynamics with surfactants remains a challenging task. The first challenge comes from the modelling of interfacial dynamics with surfactants. The presence of surfactants brings some difficulties to simulations (Booty & Siegel 2010; Zhang et al. 2014; Liu et al. 2018), including (1) a suitable equation of state is needed to account for the effect of surfactants in reducing the interfacial tension; (2) in addition to the hydrodynamic equations, an advection-diffusion equation should be introduced to describe the evolution of surfactant concentration (Khatri & Tornberg 2014); (3) the non-uniform distribution of surfactants along the interface creates the Marangoni stress, and this effect should be considered in the governing system; (4) for soluble surfactants, adsorption and desorption of surfactants on the interface further increase the difficulty of modelling(Cuenot et al. 1997). To address these difficulties, numerous numerical methods have been developed, such as the level set method (Xu et al. 2012; Xu & Ren 2014; Titta et al. 2018), the volume of fluid method (Alke & Bothe 2009; James & Lowengrub 2004), the front tracking method (Zhang et al. 2006; Muradoglu & Tryggvason 2008), the immersed boundary method (Lai et al. 2010) and the lattice Boltzmann method (Van der Sman & Van der Graaf 2006; Zhang et al. 2015; Zhao et al. 2018; Wei et al. 2019). Although these methods have made great progresses in simulating interfacial flows with surfactants, they still suffer from several drawbacks (Liu et al. 2018), including (1) the level set and VOF methods require either unphysical re-initialization processes or complex interface reconstruction algorithms to represent the interface and surfactant concentration; (2) the front tracking and immersed boundary methods have difficulty in dealing with large topological changes, for example, the droplet breakup and coalescence; (3) most lattice Boltzmann models do not consider the Marangoni stress (Liu et al. 2018), which is unphysical and could have an important impact on the droplet dynamics. The second challenge is the MCL problem. It is well known that under the usual hydrodynamic assumptions, namely the incompressible Navier–Stokes equations and no-slip boundary condition, non-physical singularities will occur in the vicinity of the MCL, and the velocity field is multi-valued at the contact line (Wang et al. 2008; Xu et al. 2018). To remove the singularities at the MCL, various continuous models have been proposed, and reviews of these models can refer to Snoeijer and Andreotti (2013) and Sui et al. (2014). Among these models, the Navier boundary condition (NBC) is a classical and natural boundary condition (Yang 2017; Alpak et al. 2018; Zampogna et al. 2019), and it has been used in simulations of contact line dynamics

with insoluble surfactants. Lai et al. (2010) used an immersed boundary method to simulate the MCL problem, and studied the effect of insoluble surfactants on contact angles. A level set method for two-phase flows with the MCL and insoluble surfactants was proposed by Xu and Ren (2014). Zhang et al. (2014) derived a continuous model for the dynamics of two immiscible fluids with the MCL and insoluble surfactants based on thermodynamic principles. Their pioneering studies have greatly promoted the development of simulations for the droplet dynamics with the MCL and surfactants. However, the dynamic contact line condition and soluble surfactants are not considered in these studies.

Recently, the phase-field model has shown great potential for the modelling of two-phase flows with the MCL and surfactants. In this model, the interface is treated as a thin diffuse layer between different fluids represented by a phase-field variable (Shen & Yang 2015; Alpak et al. 2016; Frank et al. 2018; Kou & Sun 2018a; Kou & Sun 2018b). Compared with sharp interface models, the phase-field model has several obvious advantages, including (1) it does not need to track the interface explicitly, and the interface is captured implicitly and automatically by the evolution of phase-field variable (Xu et al. 2018). Thus, computations and analysis for the phase-field model are much easier than other methods; (2) the phase-field model has a firm physical basis for multiphase flow (Liu & Zhang 2010; Chen et al. 2014), since the governing system can be derived from an energy-based variational formalism, and the developed model normally satisfies thermodynamically consistent energy dissipation law (Shen & Yang 2015; Yang et al. 2017; Zhu et al. 2019a). These advantages make the phase-field model widely used to simulated interfacial phenomena, e.g., surfactant-driven interfacial flows (Teigen et al. 2011; Yun et al. 2014). Laradji et al. (1992) proposed the first phase-field surfactant model. In their pioneering work, two phase-field variables were introduced in the free energy functional, which formed the general framework of phase-field surfactant models, to represent fluid components and surfactant concentration, respectively. Since then, numerous phase-field surfactant models (Copetti & Elliott 1992; Komura & Kodama 1997; Van der Sman & Van der Graaf 2006) have been proposed and reviews of these models can be found in Li and Kim (2012); Yang and Ju (2017); Zhu et al. (2018). In this study, we adopt a typical representative of phase-field surfactant model (free energy functional) developed by Engblom et al. (2013). In the proposed free energy functional, the classical Cahn–Hilliard potential determines the dynamics of diffuse interface, and the logarithmic Floy-Huggins potential controls the entropy of mixing surfactants with the bulk phases and restricts the range of concentration variable. The nonlinearly coupled surface energy potential locally attracts surfactants to the interface of fluids, while the enthalpic term globally penalizes free surfactants in the bulk phases and stabilizes the phase-field model. Recently, we coupled this model with the hydrodynamic equations to simulate the interfacial flows with surfactants. Several linear, decoupled and energy stable schemes were also constructed to solve this complex system effectively (Zhu et al. 2019b). Our three-dimensional (3D) results successfully demonstrate the effect of surfactants on the interfacial dynamics. To date, a series of hydrodynamics coupled phase-field surfactant models have been developed (Pätzold & Dawson 1995; Liu & Zhang 2010; Teigen et al. 2011; Garcke et al. 2013), but none of them has considered the MCL problem. Hence, it is necessary to extend our current work to the modelling of MCL problem.

Although the no-slip velocity boundary condition leads to the well-known contact line paradox for sharp interface models, it works well for the phase-field model. The chemical diffusion in the thin interface, arising from the non-equilibrium of chemical potential, can cause the motion of

contact line. Hence, the singularities at the MCL can be successfully removed in the phase-field model when a no-slip boundary condition is imposed. On the other hand, a slip boundary condition also works well for the phase-field model. Using careful molecular dynamics studies of the slip behavior near the MCL (Qian et al. 2004; Qian et al. 2006) and principles of thermodynamic, Qian et al. (2003) proposed a generalized Navier boundary condition (GNBC). The GNBC states that the slip velocity at the MCL is proportional to the sum of viscous stress and unbalanced Young stress; the latter arises from the deviation of the fluid-fluid interface from its equilibrium configuration (Wang et al. 2008). They further demonstrated that the GNBC can quantitatively reproduce the MCL slip velocity profiles obtained by molecular dynamics simulations (Qian et al. 2006). The GNBC can reduce to the typical NBC (Fan et al. 2019) in equilibrium, and the NBC would reduce to the no-slip boundary condition when the slip length of fluid on the solid substrate is zero (Yu & Yang 2017). For the wetting boundary condition, the GNBC uses the typical surface-energy approach (Jacqmin 2000; Frank et al. 2018) to prescribe a dynamic contact angle between the diffuse interface and solid substrate. Note that there are also some other well-known approaches to describe contact angles in the framework of the phase-field model, for example, the geometric contact angle approach derived by Ding and Spelt (2007) and the extended geometric approach developed by Alpak et al. (2016). The GNBC shows great advantages and prospects in simulating the MCL dynamics, and several attempts have been made to develop energy stable schemes for the GNBC-based phase-field models. In this work, the GNBC is adopted to handle the slip boundary condition and dynamic contact angle at the fluid-solid interface.

As a first attempt, we present a derivation of the phase-field MCL model with soluble surfactants through the first law of thermodynamics, related thermodynamical relations and the Onsager's variational principle. The derived thermodynamically consistent model consists of two Cahn–Hilliard–type equations governing the evolution of interface and surfactant concentration, the incompressible Navier–Stokes equations and the GNBC for the MCL. With chemical potentials derived from the free energy functional, we analytically obtain certain equilibrium properties of surfactant adsorption, including equilibrium profiles for phase-field variables, the Langmuir isotherm and the equilibrium equation of state. A classical droplet spread case is used to numerically validate the MCL model and equilibrium properties of surfactant adsorption. Using the proposed model, we investigate the droplet dynamics with soluble surfactants on a chemically patterned surface.

2. Derivation of moving contact line hydrodynamics with surfactants

In this section, we will present a derivation of the phase-field MCL model with soluble surfactants. The governing equation is derived through three key steps, including (1) the first law of thermodynamics and related thermodynamical relations are used to derive an entropy equation; (2) the momentum equation and the slip boundary condition are obtained through the Galilean invariance; (3) the Onsager's variational principle is used to obtain diffusive fluxes and the stress tensor. The derived model consists of two Cahn–Hilliard–type equations for phase-field variables, the incompressible Navier–Stokes equations, and the GNBC for the MCL.

2.1. Free energy functional and entropy equation

In an immiscible two-phase system with soluble surfactants, there are three types of free energy, including the mixing energy, free energies associated with surfactants, and the surface energy at the fluid-solid interface.

Mixing energy. In the phase-field model, a phase-field variable is introduced to distinguish two phases, and the interface is treated as a thin and continuous layer, inside which the two phases are mixed and store the mixing energy. The classical Cahn–Hilliard free energy functional (Gao & Wang 2012; Engblom et al. 2013) is used to represent the mixing energy

$$F_{mix}(\phi)=\int\left[-\frac{A}{2}\phi^2+\frac{B}{4}\phi^4+\frac{A}{4}+\frac{\kappa}{2}|\nabla\phi|^2\right]\mathrm{d}\Omega, \tag{2.1}$$

where ϕ is the phase-field variable measuring the local composition of fluids. Parameters A, B and κ can be determined from the two equilibrium phases $\phi_{\pm}=\pm\sqrt{A/B}$, and the interfacial thickness parameter $\varepsilon=\sqrt{\kappa/A}$. The polynomial part $-A\phi^2/2+B\phi^4/4+A/4$ in F_{mix} prefers the total separation of two phases and produces the classical sharp-interface picture (Yue et al. 2004). The square gradient term $\kappa|\nabla\phi|^2/2$ represents weakly non-local interactions between fluids that prefers the complete mixing of phases. The competition between two terms leads to a diffuse interface in equilibrium (Shen & Yang 2015), where F_{mix} reaches the minimum.

Free energies associated with surfactants. The presence of surfactants would greatly affect the dynamics of fluid mixtures. To account for the effect of surfactants, additional energy terms are introduced to the Cahn–Hilliard free energy functional, including a logarithmic free energy, a nonlinearly coupled surface energy and an energy term measuring the cost of free surfactants.

F_1 is a typical logarithmic free energy (Yang & Ju 2017) governing the entropy of mixing surfactants with the bulk phases

$$\begin{cases}F_1(\psi)=\int\left[k_bT_eG(\psi)\right]\mathrm{d}\Omega,\\ G(\psi)=\psi\ln\psi+(1-\psi)\ln(1-\psi),\end{cases} \tag{2.2}$$

where ψ is a phase-field variable representing the surfactant concentration, k_b is the Boltzmann constant and T_e denotes the temperature. The constant k_bT_e takes the role of a diffusion coefficient for ψ at the given temperature. The first term $\psi\ln\psi$ in the Flory-Huggins potential $G(\psi)$ models the ideal mixing of surfactants in the bulk phases and guarantees the value of ψ to be positive, and the second term $(1-\psi)\log(1-\psi)$ restricts $\psi<1$. Thus, the surfactant concentration ψ varies within the range of 0 and 1 in this study.

Surfactants can automatically absorb onto the interface and form a buffer zone to reduce the system energy. A surface energy F_2 (Engblom et al. 2013) is adopted to account for the high surfactant concentration near the interface

$$F_2(\phi,\psi)=\int\left[-\frac{\zeta}{4}\psi\left(1-\phi^2\right)^2\right]\mathrm{d}\Omega. \tag{2.3}$$

Here we set $\zeta=A$ to reduce unnecessary free parameters (Engblom et al. 2013). Theoretically, the surface energy F_2 is inactive in the bulk phases and reaches the minimum on the interface. The energy term F_3 is used to penalize free surfactants in the bulk phases,

$$F_3(\phi,\psi)=\int\left[\frac{W}{2}\psi\phi^2\right]\mathrm{d}\Omega, \tag{2.4}$$

where W is a positive parameter. F_3 also plays a significant role in stabilizing the phase-field model (Liu & Zhang 2010). It is obviously that F_3 is inactive on the interface where $\phi\approx 0$ and reaches the maximum in the bulk phases. To some extent, F_2 and F_3 are complementary: F_2 locally attracts

surfactants to the interface while F_3 globally counteracts the occurrence of free surfactants (Engblom et al. 2013).

Surface energy at the fluid-solid interface. When the diffuse interface touches a solid surface, the MCL problem occurs. The interfacial free energy per unit area $M(\phi)$ at the fluid-solid interface is determined by the interfacial tension σ between fluids, the contact angle θ_s between the diffuse interface and solid surface, and the local composition of fluids ϕ on the solid surface. The typical free energy at the fluid-solid surface (Gao & Wang 2014) reads

$$F_{wf}(\phi) = \int M(\phi)\,\mathrm{dS} = \int\left[-\frac{\sigma}{2}\cos\theta_s \sin\left(\frac{\pi}{2}\phi\right)\right]\mathrm{dS}. \tag{2.5}$$

The total free energy F of a two-phase system with soluble surfactants can be written as the sum of the mixing energy, free energies associated with surfactants and the free energy at the fluid-solid interface:

$$F(\phi,\psi) = F_{mix}(\phi) + F_1(\psi) + F_2(\phi,\psi) + F_3(\phi,\psi) + F_{wf}(\phi). \tag{2.6}$$

Three quantities w_ϕ, w_ψ and L can be variationally derived from the total free energy F

$$\delta F(\phi,\psi) = \int\left[w_\phi\,\delta\phi\right]\mathrm{d}\Omega + \int\left[w_\psi\,\delta\psi\right]\mathrm{d}\Omega + \int\left[L\,\delta\phi\right]\mathrm{dS}, \tag{2.7}$$

where w_ϕ is the chemical potential determining the composition diffusion

$$w_\phi = -A\phi + B\phi^3 - \kappa\Delta\phi + W\psi\phi - \zeta\psi\phi\left(\phi^2 - 1\right). \tag{2.8}$$

Equation (2.8) indicates that the surfactant concentration may greatly affect the composition diffusion, and change the equilibrium profile of the phase-field variable ϕ. The detailed discussion about this issue will be presented in Section 3. w_ψ is the chemical potential governing the diffusion of surfactants

$$w_\psi = k_b T_e \ln\left(\frac{\psi}{1-\psi}\right) + \frac{W}{2}\phi^2 - \frac{\zeta}{4}\left(\phi^2 - 1\right)^2, \tag{2.9}$$

and L is the chemical potential at the solid surface

$$L = \kappa\partial_n\phi + M'(\phi). \tag{2.10}$$

By minimizing the total free energy F with respect to phase-field variables ϕ and ψ, we can obtain equilibrium conditions, where chemical potentials are constants throughout the whole system. Deviations from equilibrium conditions, measured by the chemical potential gradients ∇w_ϕ and ∇w_ψ in the bulk phases and L at the fluid-solid interface (Qian et al. 2006), will lead to the composition diffusion, the surfactant diffusion in the bulk phases and the relaxation at the fluid-solid interface. The conservation of ϕ and ψ requires that diffusive fluxes and material derivatives of phase-field variables satisfy the continuity equation, namely

$$\dot{\phi} = \phi_t + \mathbf{u}\cdot\nabla\phi = -\nabla\cdot\mathbf{J}_\phi, \tag{2.11}$$

and

$$\dot{\psi} = \psi_t + \mathbf{u}\cdot\nabla\psi = -\nabla\cdot\mathbf{J}_\psi, \tag{2.12}$$

where $\mathbf{J}_\phi$ and $\mathbf{J}_\psi$ are diffusive fluxes resulting from the composition diffusion and surfactant

diffusion, respectively. $\mathbf{u}$ is the flow velocity field. The relaxation arising from L can be described by the material derivative ϕ at the solid surface, i.e., $\dot{\phi} = \phi_t + \mathbf{u}_\tau \partial_\tau \phi$, where $\mathbf{u}_\tau$ is the tangential velocity of fluid on the solid surface. The mass conservation of system requires that

$$\dot{\rho} = \rho_t + \mathbf{u} \cdot \nabla \rho = -\nabla \cdot \mathbf{J}, \tag{2.13}$$

where ρ is the fluid density, and $\mathbf{J}$ is the diffusive mass flux, which is determined by the diffusive flux $\mathbf{J}_\phi$ and density difference between fluids.

Now we will combine the first law of thermodynamics and classical thermodynamical relations to derive the entropy balance equation. Then, we can obtain the momentum equation and the slip boundary condition using the Galilean invariance.

Similar to the variation of the total free energy F, the rate of change of F can be written as

$$\dot{F} = \int \left[w_\phi \phi_t \right] \mathrm{d}\Omega + \int \left[w_\psi \psi_t \right] \mathrm{d}\Omega + \int \left[L \phi_t \right] \mathrm{dS}. \tag{2.14}$$

Substituting (2.11), (2.12) and $\phi_t = \dot{\phi} - \mathbf{u}_\tau \partial_\tau \phi$ into (2.14), we obtain

$$\dot{F} = \int \left[-w_\phi \nabla \cdot \mathbf{J}_\phi - w_\phi \mathbf{u} \cdot \nabla \phi \right] \mathrm{d}\Omega + \int \left[-w_\psi \nabla \cdot \mathbf{J}_\psi - w_\psi \mathbf{u} \cdot \nabla \psi \right] \mathrm{d}\Omega + \int \left[L \left(\dot{\phi} - \mathbf{u}_\tau \partial_\tau \phi \right) \right] \mathrm{dS} \tag{2.15}$$

Considering the fact that normal diffusion fluxes disappear at the solid surface because of the impermeability condition, specifically, $\mathbf{J}_\phi \cdot \mathbf{n}\big|_{\mathrm{S}} = 0$ and $\mathbf{J}_\psi \cdot \mathbf{n}\big|_{\mathrm{S}} = 0$, we obtain identities

$$-\int \left[w_\phi \nabla \cdot \mathbf{J}_\phi \right] \mathrm{d}\Omega = -\int \left[w_\phi \mathbf{J}_\phi \cdot \mathbf{n} \right] \mathrm{dS} + \int \left[\nabla w_\phi \cdot \mathbf{J}_\phi \right] \mathrm{d}\Omega = \int \left[\nabla w_\phi \cdot \mathbf{J}_\phi \right] \mathrm{d}\Omega \tag{2.16}$$

and $-\int \left[w_\psi \nabla \cdot \mathbf{J}_\psi \right] \mathrm{d}\Omega = \int \left[\nabla w_\psi \cdot \mathbf{J}_\psi \right] \mathrm{d}\Omega$. Similarly, we can obtain $-\int \left[w_\phi \mathbf{u} \cdot \nabla \phi \right] \mathrm{d}\Omega = \int \left[\phi \mathbf{u} \cdot \nabla w_\phi \right] \mathrm{d}\Omega$ and $-\int \left[w_\psi \mathbf{u} \cdot \nabla \psi \right] \mathrm{d}\Omega = \int \left[\psi \mathbf{u} \cdot \nabla w_\psi \right] \mathrm{d}\Omega$ using the boundary condition $\mathbf{u} \cdot \mathbf{n}\big|_{\mathrm{S}} = 0$, where $\mathbf{n}$ is the unit vector orthogonal to boundaries. Then (2.15) can be rewritten as

$$\dot{F} = \int \left[\nabla w_\phi \cdot \mathbf{J}_\phi + \nabla w_\psi \cdot \mathbf{J}_\psi \right] \mathrm{d}\Omega + \int \left[\phi \mathbf{u} \cdot \nabla w_\phi + \psi \mathbf{u} \cdot \nabla w_\psi \right] \mathrm{d}\Omega + \int \left[L \dot{\phi} - L \mathbf{u}_\tau \partial_\tau \phi \right] \mathrm{dS}. \tag{2.17}$$

The first law of thermodynamics states

$$\left(\dot{U} + \dot{E}_k \right) = \dot{W} + \dot{Q}, \tag{2.18}$$

where U is the internal energy, W is the work done by the face force F_t, and Q denotes the heat from the surrounding that keep the system temperature constant. E_k is the kinetic energy, and it is defined as $E_k = \frac{1}{2} \int \left[\rho |\mathbf{u}|^2 \right] \mathrm{d}\Omega$. The total entropy S is contributed by two components, including (I) the entropy of system S_{sys}; (II) the entropy of the surrounding S_{surr}, which has the relation with Q as $\dot{S}_{\mathrm{surr}} = -\dot{Q}/T$. Using the thermodynamical relation $\dot{U} = \dot{F} + T\dot{S}_{\mathrm{sys}}$, we have

$$\dot{S} = \dot{S}_{\mathrm{sys}} + \dot{S}_{\mathrm{surr}} = \dot{S}_{\mathrm{sys}} - \frac{\dot{Q}}{T} = -\frac{1}{T} \left(\dot{F} + \dot{E}_k \right) + \frac{1}{T} \dot{W}. \tag{2.19}$$

Applying the Reynolds transport theorem and the Gauss divergence theorem, we can derive that

$$\begin{aligned} \dot{E}_k &= \frac{1}{2} \int \left[\frac{\partial \left(\rho \mathbf{u} \cdot \mathbf{u} \right)}{\partial t} \right] \mathrm{d}\Omega + \frac{1}{2} \int \left[\nabla \cdot \left(\left[\rho \mathbf{u} \cdot \mathbf{u} \right] \mathbf{u} \right) \right] \mathrm{d}\Omega \\ &= \int \left[\rho \mathbf{u} \cdot \mathbf{u}_t + \frac{1}{2} \mathbf{u} \cdot \mathbf{u} \rho_t \right] \mathrm{d}\Omega + \frac{1}{2} \int \left[\left(\rho \mathbf{u} \cdot \mathbf{u} \right) \nabla \cdot \mathbf{u} + \left(\mathbf{u} \cdot \mathbf{u} \right) \mathbf{u} \cdot \nabla \rho + \rho \mathbf{u} \cdot \nabla \left(\mathbf{u} \cdot \mathbf{u} \right) \right] \mathrm{d}\Omega \\ &= \int \left[\mathbf{u} \cdot \left(\rho \mathbf{u}_t + \rho \mathbf{u} \cdot \nabla \mathbf{u} \right) \right] \mathrm{d}\Omega + \frac{1}{2} \int \left[\left(\mathbf{u} \cdot \mathbf{u} \right) \left(\rho_t + \mathbf{u} \cdot \nabla \rho \right) \right] \mathrm{d}\Omega. \end{aligned} \tag{2.20}$$

Substituting (2.13) into (2.20), and using integration by parts, we have

$$\dot{E}_k = \int \left[\mathbf{u} \cdot \left(\rho \mathbf{u}_t + \rho \mathbf{u} \cdot \nabla \mathbf{u} + \mathbf{J} \cdot \nabla \mathbf{u} \right) \right] \mathrm{d}\Omega. \tag{2.21}$$

The work done by the stress $\boldsymbol{\sigma}$, and the fraction force $\mathbf{f}_s$ at the fluid-solid interface is expressed as

$$\dot{W} = -\int \left[\boldsymbol{\sigma}^T : \nabla \mathbf{u} + \mathbf{u} \cdot (\nabla \cdot \boldsymbol{\sigma}) \right] \mathrm{d}\Omega + \int \left[(\boldsymbol{\sigma} \cdot \mathbf{n}) \cdot \mathbf{u}_s \right] \mathrm{dS} + \int \left[\mathbf{f}_\tau \cdot \mathbf{u}_s \right] \mathrm{dS}, \tag{2.22}$$

where $\mathbf{u}_s$ is slip velocity of fluids relative to the solid wall. Note that $\mathbf{u}_s$ is equal to $\mathbf{u}_\tau$ when the solid wall is static.

Substituting (2.17), (2.21) and (2.22) into (2.19), we can obtain the entropy balance equation

$$\begin{aligned} T\dot{S} = & -\int \left[\mathbf{u} \cdot \left(\rho \mathbf{u}_t + \rho \mathbf{u} \cdot \nabla \mathbf{u} + \mathbf{J} \cdot \nabla \mathbf{u} + \nabla \cdot \boldsymbol{\sigma} + \phi \nabla w_\phi + \psi \nabla w_\psi \right) \right] \mathrm{d}\Omega \\ & - \int \left[\boldsymbol{\sigma}^T : \nabla \mathbf{u} - \mathbf{J}_\phi \cdot \nabla w_\phi - \mathbf{J}_\psi \cdot \nabla w_\psi \right] \mathrm{d}\Omega - \int \left[L \dot{\phi} \right] \mathrm{dS} \\ & + \int \mathbf{u}_\tau \cdot \left[\boldsymbol{\sigma} \cdot \mathbf{n} + \mathbf{f}_s + L \partial_\tau \phi \right] \mathrm{dS}. \end{aligned} \tag{2.23}$$

The Galilean invariance yields from (2.23)

$$\rho \mathbf{u}_t + \rho \mathbf{u} \cdot \nabla \mathbf{u} + \mathbf{J} \cdot \nabla \mathbf{u} + \nabla \cdot \boldsymbol{\sigma} + \phi \nabla w_\phi + \psi \nabla w_\psi = 0 \tag{2.24}$$

in the bulk phases and

$$\left(\boldsymbol{\sigma} \cdot \mathbf{n} + \mathbf{f}_s + L \partial_\tau \phi \right) \cdot \boldsymbol{\tau} = 0 \tag{2.25}$$

at the fluid-solid interface. The equation (2.24) is the Navier-Stokes equation for two-phase flows with soluble surfactants, and (2.25) is the slip boundary condition. The total stress tensor $\boldsymbol{\sigma}$ can be split into $\boldsymbol{\sigma} = p\mathbf{I} + \boldsymbol{\sigma}_{\text{irrev}}$, where p is the reversible part, i.e., the pressure, and $\boldsymbol{\sigma}_{\text{irrev}}$ is the irreversible part. With the incompressibility constraint $\nabla \cdot \mathbf{u} = 0$, we can derive that

$$\boldsymbol{\sigma}^T : \nabla \mathbf{u} = p \nabla \cdot \mathbf{u} + \boldsymbol{\sigma}_{\text{irrev}}^T : \nabla \mathbf{u} = \boldsymbol{\sigma}_{\text{irrev}}^T : \nabla \mathbf{u}, \tag{2.26}$$

and (2.25) can reduce to

$$\left(\boldsymbol{\sigma}_{\text{irrev}} \cdot \mathbf{n} + \mathbf{f}_s + L \partial_\tau \phi \right) \cdot \boldsymbol{\tau} = 0. \tag{2.27}$$

Thus, the entropy balance equation (2.23) is simplified as

$$-T\dot{S} = \int \left[\boldsymbol{\sigma}_{\text{irrev}}^T : \nabla \mathbf{u} + \mathbf{J}_\phi \cdot \nabla w_\phi + \mathbf{J}_\psi \cdot \nabla w_\psi \right] \mathrm{d}\Omega + \int \left[L \dot{\phi} \right] \mathrm{dS}. \tag{2.28}$$

Next, we will use the entropy balance equation (2.28) and the dissipation function to obtain diffusive fluxes and the irreversible stress tensor.

2.2. Onsager's variational principle

An irreversible process (e.g., diffusion) taking place in a thermodynamic system leads to the dissipation, and the principle of minimum energy dissipation produces the most probable course of an irreversible process when deviations from equilibrium conditions are small. For a multiphase system with the MCL and soluble surfactants, there are several physically distinct sources of dissipations, and now we will discuss them in detail. The work done by a fluid on adjacent layers due to the action of shear force is transformed into the heat, and this irreversible process is called

the viscous dissipation. The rate of viscous dissipation in the bulk phases R_v can be written as

$$R_v(\mathbf{u}) = \int \left[\frac{\boldsymbol{\sigma}_{\text{irrev}}^2}{\eta} \right] \mathrm{d}\Omega, \tag{2.29}$$

where η is the fluid viscosity. Obviously, R_v is positive definite and quadratic in the rate $\boldsymbol{\sigma}_{\text{irrev}}$.

As we mentioned before, chemical potential gradients in the bulk phases and L at the fluid-solid interface measure deviations from equilibrium conditions. The diffusive flux $\mathbf{J}_\phi$ arising from ∇w_ϕ, the diffusive flux $\mathbf{J}_\psi$ resulting from ∇w_ψ, and the composition relaxation $\dot{\phi}$ at the solid surface coming from L are sources of additional energy dissipation. According to the general rule governing entropy production in a thermodynamic process, the addition rate of dissipation R_t should be positive definite and quadratic in the rates $\{\mathbf{J}_\phi, \dot{\phi}, \text{and } \mathbf{J}_\psi\}$, e.g., $R_t = R_d + R_{ds} + R_r$, where

$$R_d(\phi) = \int \left[\frac{\mathbf{J}_\phi^2}{M_\phi} \right] \mathrm{d}\Omega, \quad R_{ds}(\psi) = \int \left[\frac{\mathbf{J}_\psi^2}{M_\psi} \right] \mathrm{d}\Omega, \quad R_r(\phi) = \int \left[\frac{\dot{\phi}}{\Gamma} \right] \mathrm{dS},$$

here R_d comes from the composition diffusion, R_{ds} arises from the diffusion associated with surfactants, and R_r is attributed to the composition relaxation at the solid surface. M_ϕ, M_ψ and Γ are phenomenological parameters. Now we can obtain the free energy dissipation for a two-phase system with the MCL and soluble surfactants $R = R_v + R_d + R_{ds} + R_r$.

The Onsager's variation principle (Onsager 1931a; Onsager 1931b; Qian et al. 2006) states that for an open system, the state evolution equation can be obtained by minimizing $\Phi - T\dot{S}$ with respect to the rates $\{\mathbf{J}_\phi, \mathbf{J}_\psi, \dot{\phi} \text{ and } \boldsymbol{\sigma}_{\text{irrev}}\}$. Φ is the dissipation functional, which equals half free energy dissipation R

$$\Phi = \int \left[\frac{\boldsymbol{\sigma}_{\text{irrev}}^2}{2\eta} + \frac{\mathbf{J}_\phi^2}{2M_\phi} + \frac{\mathbf{J}_\psi^2}{2M_\psi} \right] \mathrm{d}\Omega + \int \left[\frac{\dot{\phi}}{2\Gamma} \right] \mathrm{dS}. \tag{2.30}$$

Adding (2.28) and (2.30) together, we have

$$\Phi - T\dot{S} = \int \left[\frac{\boldsymbol{\sigma}_{\text{irrev}}^2}{2\eta} + \frac{\mathbf{J}_\phi^2}{2M_\phi} + \frac{\mathbf{J}_\psi^2}{2M_\psi} + \boldsymbol{\sigma}_{\text{irrev}}^T : \nabla\mathbf{u} + \mathbf{J}_\phi \cdot \nabla w_\phi + \mathbf{J}_\psi \cdot \nabla w_\psi \right] \mathrm{d}\Omega + \int \left[\frac{\dot{\phi}}{2\Gamma} + L\dot{\phi} \right] \mathrm{dS}. \tag{2.31}$$

By minimizing $\Phi - T\dot{S}$ with respect to the rates $\{\mathbf{J}_\phi, \mathbf{J}_\psi, \dot{\phi} \text{ and } \boldsymbol{\sigma}_{\text{irrev}}\}$, we can obtain the phase-field MCL model with soluble surfactants.

The Euler-Lagrange equation for minimizing $\Phi - T\dot{S}$ with respect to $\mathbf{J}_\phi$ is

$$\mathbf{J}_\phi = -M_\phi \nabla w_\phi, \tag{2.32}$$

where the phenomenological parameter M_ϕ can be viewed as a mobility coefficient, and it is usually taken as a constant. The equation (2.32) indicates that the diffusive flux $\mathbf{J}_\phi$ and the chemical potential w_ϕ satisfy the classical Fick's first law. Substituting (2.32) into the continuity equation (2.11) yields the desired Cahn–Hilliard–type equation for ϕ

$$\dot{\phi} = \phi_t + \mathbf{u} \cdot \nabla\phi = -\nabla \cdot \mathbf{J}_\phi, = \nabla \cdot M_\phi \nabla w_\phi. \tag{2.33}$$

Similarly, we can obtain the Cahn–Hilliard–type equation for ψ

$$\dot{\psi} = \psi_t + \mathbf{u}\cdot\nabla\psi = -\nabla\cdot\mathbf{J}_\psi, = \nabla\cdot M_\psi\nabla w_\psi. \tag{2.34}$$

To combine with the logarithmic chemical potential w_ψ, the mobility coefficient M_ψ for ψ usually takes the form of $m_\psi\psi(1-\psi)$, where m_ψ is a constant. M_ψ vanishes at the extreme points ψ =0 and ψ =1. Substituting M_ψ into equation (2.34), and using equation (2.9), we have

$$\psi_t + \mathbf{u}\cdot\nabla\psi = \nabla\cdot\left(M_\psi\frac{\partial w_\psi}{\partial\psi}\nabla\psi\right) = \nabla\cdot\left(M_\psi\frac{k_bT_e}{\psi(1-\psi)}\nabla\psi\right) = \nabla\cdot\left(m_\psi k_bT_e\nabla\psi\right) = \nabla\cdot\left(D_\psi\nabla\psi\right),$$

where D_ψ can be seen as the surfactant diffusive coefficient in the bulk phases. Then (2.34) is translated into the widely used bulk surfactant transport equation in sharp interface models.

By minimizing $\Phi - TS$ with respect to $\dot{\phi}$ at the fluid-solid interface, we have

$$\dot{\phi} = \phi_t + \mathbf{u}_\tau\partial_\tau\phi = -\Gamma L. \tag{2.35}$$

The equation (2.35) is the dynamic contact line condition. It can be observed that the relaxation dynamics for ϕ at the fluid-solid interface is proportional to the deviation of L from its equilibrium value zero.

Considering the variation of $\Phi - TS$ with respect to $\boldsymbol{\sigma}_{\text{irrev}}$, we have

$$\boldsymbol{\sigma}_{\text{irrev}} = -\eta\nabla\mathbf{u}. \tag{2.36}$$

Substituting (2.36) into (2.24), we obtain the desired Navier-Stokes equation for two-phase flows with soluble surfactants

$$\rho\mathbf{u}_t + \rho\mathbf{u}\cdot\nabla\mathbf{u} + \mathbf{J}\cdot\nabla\mathbf{u} - \eta\Delta\mathbf{u} + \phi\nabla w_\phi + \psi\nabla w_\psi = 0. \tag{2.37}$$

Note that the viscous term $\eta\Delta\mathbf{u}$ can be readily generalized to $\nabla\cdot\eta D(\mathbf{u})$ if $\boldsymbol{\sigma}_{\text{irrev}}$ is symmetric, where $D(\mathbf{u}) = \nabla\mathbf{u} + \nabla^T\mathbf{u}$. For two phases with variable densities and viscosities, the density ρ and viscosity η usually have the following linear relations

$$\rho = \frac{\rho_1-\rho_2}{2}\phi + \frac{\rho_1+\rho_2}{2}, \quad \eta = \frac{\eta_1-\eta_2}{2}\phi + \frac{\eta_1+\eta_2}{2}. \tag{2.38}$$

Substituting the density equation in (2.38) into the Cahn–Hilliard–type equation for ϕ, and using the incompressibility constraint $\nabla\cdot\mathbf{u} = 0$, we get

$$\mathbf{J} = \frac{\rho_2-\rho_1}{2}M_\phi\nabla w_\phi = \frac{\rho_1-\rho_2}{2}\mathbf{J}_\phi. \tag{2.39}$$

We naturally assume that the fraction force is linear to the slip velocity of fluids $\mathbf{u}_s$, i.e., $\mathbf{f}_s = -\beta\mathbf{u}_s$, where β is the slip coefficient and it can be used to define a slip length $l_s = \eta/\beta$. Substituting (2.36) into (2.27), we obtain

$$\beta\mathbf{u}_s = -\eta\partial_n\mathbf{u}_\tau + L\partial_\tau\phi \tag{2.40}$$

at the fluid-solid interface. The unbalanced Young stress $L\partial_\tau\phi$ and $\eta\partial_n\mathbf{u}_\tau$ in (2.40) are manifestations of the interfacial tension and the viscous stress at the solid surface, respectively. In general, we denote the dynamic contact line condition (2.35) and the slip boundary condition (2.40) together as the GNBC.

When the relaxation parameter Γ in equation (2.35) tends to infinity, the dynamic contact line condition reduces to the static contact line condition as

$$L = \kappa\partial_n\phi + M'(\phi) = 0, \tag{2.41}$$

and the slip boundary condition (2.40) becomes $\beta\mathbf{u}_s = -\eta\partial_n\mathbf{u}_\tau$, which is the well-known NBC. The contact line effect disappears if we further set $M'(\phi) = 0$ in equation (2.41). As the slip length l_s ($l_s = \eta/\beta$) approaches zero, the NBC reduces to the traditional no-slip boundary condition. In the other limit, l_s approaches infinity, the tangential viscous stress on the boundary disappears. Thus the NBC interpolates between the no-slip limit and the zero–tangential–viscous–stress limit (Qian et al. 2006).

Two Cahn–Hilliard–type equations for phase-field variables, the incompressible Navier–Stokes equation, and the GNBC for the MCL form the phase-field MCL model with soluble surfactants.

2.3. Dimensionless governing equation and numerical scheme

We use a global characteristic length scale L_c, a characteristic velocity U_c and properties (density ρ_1 and viscosity η_1) of fluid I to define some dimensionless parameters. With defined parameters, we obtain dimensionless Cahn–Hilliard–type equations

$$\psi_t + \nabla\cdot(\mathbf{u}\psi) = \frac{1}{\mathrm{Pe}_\psi}\nabla\cdot M_d\nabla w_\psi, \tag{2.42}$$

$$w_\psi = \mathrm{Pi}\ln\left(\frac{\psi}{1-\psi}\right) + \frac{1}{2\mathrm{Ex}}\phi^2 - \frac{\left(\phi^2-1\right)^2}{4}, \tag{2.43}$$

$$\phi_t + \nabla\cdot(\mathbf{u}\phi) = \frac{1}{\mathrm{Pe}_\phi}\Delta w_\phi, \tag{2.44}$$

$$w_\phi = -\phi + \phi^3 - \mathrm{Cn}^2\Delta\phi + \frac{1}{\mathrm{Ex}}\psi\phi - \psi\phi\left(\phi^2-1\right). \tag{2.45}$$

where $M_d = \psi(1-\psi)$. The dimensionless Navier–Stokes equations are

$$\rho\mathbf{u}_t + \rho\mathbf{u}\cdot\nabla\mathbf{u} + \mathbf{J}\cdot\nabla\mathbf{u} - \frac{1}{\mathrm{Re}}\nabla\cdot\eta D(\mathbf{u}) + \nabla p + \frac{1}{\mathrm{Re}\,\mathrm{Ca}\mathrm{Cn}}\left(\phi\nabla w_\phi + \psi\nabla w_\psi\right) = 0, \tag{2.46}$$

$$\nabla\cdot\mathbf{u} = 0, \tag{2.47}$$

where

$$\mathbf{J} = \frac{\lambda_\rho - 1}{2\mathrm{Pe}_\phi}\nabla w_\phi, \quad \rho = \frac{1-\lambda_\rho}{2}\phi + \frac{1+\lambda_\rho}{2}, \quad \eta = \frac{1-\lambda_\eta}{2}\phi + \frac{1+\lambda_\eta}{2}. \tag{2.48}$$

The impermeability boundary condition of the solid surface is

$$\partial_n\psi = 0, \quad \partial_n w_\phi = 0, \quad \partial_n w_\psi = 0, \quad \mathbf{u}\cdot\mathbf{n} = 0, \quad \text{on S}. \tag{2.49}$$

The dimensionless dynamic contact line condition for ϕ at the solid surface is

$$\phi_t + \mathbf{u}_\tau\cdot\partial_\tau\phi = -\frac{1}{\mathrm{Pe}_s}L, \quad \text{on S}, \tag{2.50}$$

where $L = \mathrm{Cn}\partial_n\phi + M'(\phi)$ and $M(\phi) = -\frac{\sqrt{2}}{3}\cos\theta_s\sin\left(\frac{\pi\phi}{2}\right)$. The slip boundary condition can be written as

$$\frac{\mathrm{Ca}\eta}{L_s}\mathbf{u}_s = -\mathrm{Ca}\eta\,\partial_n\mathbf{u}_\tau + L\partial_\tau\phi, \quad \text{on S}. \tag{2.51}$$

Several dimensionless parameters are used in the above governing equation. There are (1) the Reynolds number $\mathrm{Re} = \rho_1 L_c U_c/\eta_1$, (2) the capillary number $\mathrm{Ca} = 2\sqrt{2}\eta_1 U_c/3\sigma$, (3) the Cahn number

$\mathrm{Cn}=\varepsilon/L_c$, (4) Péclet numbers $\mathrm{Pe}_\phi=L_cU_c/\left(M_\phi A\right)$ and $\mathrm{Pe}_\psi=L_cU_c/\left(m_\psi A\right)$, (5) $\mathrm{Pe}_s=U_c\mathrm{Cn}/(\kappa\Gamma)$, (6) $\mathrm{Ex}=\kappa/\left(W\varepsilon^2\right)$, which determines the bulk solubility, (7) $\mathrm{Pi}=k_bT_e/\left(A\phi_\pm^2\right)$, which is a temperature-dependent constant, (8) the slip length $L_s=\eta/\left(\beta L_c\right)$, (9) the density ratio $\lambda_\rho=\rho_2/\rho_1$ and viscosity ratio $\lambda_\eta=\eta_2/\eta_1$.

If we consider the extra body force in the momentum equation, e.g., the gravitational force, (2.46) can be modified into

$$\rho\mathbf{u}_t+\rho\mathbf{u}\cdot\nabla\mathbf{u}+\mathbf{J}\cdot\nabla\mathbf{u}-\frac{1}{\mathrm{Re}}\nabla\cdot\eta D(\mathbf{u})+\nabla p+\frac{1}{\mathrm{BoCn}}\left(\phi\nabla w_\phi+\psi\nabla w_\psi\right)-\rho\mathbf{g}=0,$$

where Bo is the Bond number, and $\mathbf{g}$ is the unit vector denoting the direction of body force.

The governing system (2.42) – (2.51) satisfies the following energy dissipation law:

$$\begin{aligned}\dot{F}_{tot}(\mathbf{u},\phi,\psi)=&-\frac{1}{\mathrm{Pe}_\phi}\left\|\nabla w_\phi\right\|^2-\frac{1}{\mathrm{Pe}_\psi}\left\|\sqrt{m_\psi}\nabla w_\psi\right\|^2-\frac{\mathrm{CaCn}}{2}\left\|\sqrt{\eta}D(\mathbf{u})\right\|^2\\&-\frac{\mathrm{Cn}}{\mathrm{Pe}_s}\|L\|_S^2-\frac{\mathrm{CaCn}}{L_s}\left\|\sqrt{\eta}\mathbf{u}_s\right\|_S^2\le 0.\end{aligned}\tag{2.52}$$

where F_{tot} is the dimensionless total energy, which is the sum of the kinetic energy and the total free energy F

$$\begin{aligned}F_{tot}(\mathbf{u},\phi,\psi)=&\int_\Omega\left(\frac{\mathrm{ReCaCn}}{2}\rho|\mathbf{u}|^2+\frac{\mathrm{Cn}^2}{2}|\nabla\phi|^2+\frac{\left(\phi^2-1\right)^2}{4}+\mathrm{Pi}G(\psi)-\frac{\psi\left(\phi^2-1\right)^2}{4}+\frac{\psi\phi^2}{2\mathrm{Ex}}\right)\mathrm{d}\Omega\\&+\mathrm{Cn}\int_S M(\phi)\,\mathrm{dS}.\end{aligned}\tag{2.53}$$

Physically, the energy dissipation law (2.52) states that the total energy of a two-phase system with the MCL and soluble surfactants will decrease from the internal dissipation. Note that the energy dissipation law in (2.52) is actually guaranteed as a part of the thermodynamic consistency by the Onsager's variational principle.

The nonlinearly coupled governing system (2.42) – (2.51) can be transformed into an equivalent one by introducing appropriate scalar auxiliary variables (SAV), and nonlinear potentials, e.g., the double well potential and the logarithmic Flory-Huggins potential, are then treated semi-explicitly (Shen et al. 2018; Kou et al. 2018; Zhu et al. 2018). For the stress and convection terms, which come from the nonlinear couplings between phase-field variables and velocity, we use some subtle implicit-explicit treatments to them (Yu & Yang 2017). For the Navier-Stokes equation, a splitting method based on the pressure stabilization is implemented to decouple the computation of velocity from pressure (Guermond & Salgado 2009; Shen & Yang 2015). A stabilization term is artificially added to balance the explicit nonlinear term associated with the surface energy at the fluid-solid interface (Shen et al. 2015). We use a finite difference method on staggered grids to complete the spatial discretization (Chen et al. 2017; Malan et al. 2019; Aniszewski et al. 2019). Note that advection terms in the Cahn-Hilliard and Navier-Stokes equations are discretized by the MINMOD scheme (Li et al. 2015; Moukalled et al. 2016; Liu et al. 2019), which is a combination of the central difference, first-order and second-order upwind schemes. The MINMOD scheme not only achieves the second-order accuracy in space, but also preserves the physical properties of convection. Other spatial derivatives are discretized using the standard central difference schemes. A preconditioned biconjugate gradient stabilized method (BICGSTAB) is used to solve the above

variables(Yan et al. 2019; Zeng et al. 2019).

3. Equilibrium properties of surfactant adsorption

In equilibrium, chemical potentials throughout the whole system are constants. Using this fact, we can obtain certain equilibrium properties and adsorption isotherm relation, including equilibrium profiles for phase-field variables, the Langmuir isotherm and the equilibrium equation of state. We first consider the equilibrium profile for ϕ at constant surfactant concentration. For a two-phase system without surfactants, the chemical potential w_ϕ reads:

$$w_\phi = -\phi + \phi^3 - \mathrm{Cn}^2 \Delta\phi, \tag{3.1}$$

and the equilibrium profile for ϕ can be written as

$$\phi(x) = \tanh\left(x \Big/ \left[\sqrt{2}\mathrm{Cn} \right] \right). \tag{3.2}$$

We denote ψ_b and ϕ_b as the surfactant bulk concentration and phase bulk value, respectively. ψ_b is far smaller than 1 ($\psi_b << 1$). Considering the fact that the chemical potential w_ϕ is equal throughout the system, we have

$$w_\phi = -\phi + \phi^3 - \mathrm{Cn}^2 \Delta\phi + \frac{1}{\mathrm{Ex}} \psi_b \phi - \psi_b \phi \left(\phi^2 - 1 \right) = 0. \tag{3.3}$$

The equation (3.3) can be rewritten as

$$\begin{aligned} w_\phi &= -\left(1 + \frac{1}{\mathrm{Ex}} - \frac{1}{\mathrm{Ex}\left(1-\psi_b\right)} \right) \phi + \phi^3 - \frac{\mathrm{Cn}^2}{1-\psi_b} \Delta\phi \\ &= -\left(1 + \frac{1}{\mathrm{Ex}} - \frac{1}{\mathrm{Ex}\left(1-\psi_b\right)} \right) \phi_b^3 \phi_b^{-2} \left(\phi_b^{-1}\phi \right) + \phi_b^3 \left(\phi_b^{-1}\phi \right)^3 - \phi_b^3 \frac{\mathrm{Cn}^2}{\phi_b^2 \left(1-\psi_b\right)} \Delta\left(\phi_b^{-1}\phi \right). \end{aligned} \tag{3.4}$$

We can further reformulate (3.4) as

$$w_\phi = \phi_b^3 \left[-\left(\phi_b^{-1}\phi \right) + \left(\phi_b^{-1}\phi \right)^3 - \mathrm{Cn}_\psi^2 \Delta\left(\phi_b^{-1}\phi \right) \right], \tag{3.5}$$

by using

$$\phi_b^2 := 1 + \frac{1}{\mathrm{Ex}} - \frac{1}{\mathrm{Ex}\left(1-\psi_b\right)}, \quad \mathrm{Cn}_\psi^2 := \frac{\mathrm{Cn}^2}{\phi_b^2 \left(1-\psi_b\right)}.$$

The equation (3.5) has the similar form with (3.1). Referring to (3.2), the equilibrium profile for the scaled variable $\phi_b^{-1}\phi$ can be written as $\phi_b^{-1}\phi = \tanh\left(x \Big/ \sqrt{2}\mathrm{Cn}_\psi \right)$. Replacing Cn_ψ with Cn, we obtain

$$\phi(x) = \phi_b \tanh\left(\phi_b \sqrt{1-\psi_b}\, \frac{x}{\sqrt{2}\mathrm{Cn}} \right), \tag{3.6}$$

with

$$\phi_b^2 = 1 + \frac{1}{\mathrm{Ex}} - \frac{1}{\mathrm{Ex}\left(1-\psi_b\right)}. \tag{3.7}$$

Using (3.6) and (3.7), we can derive the gradient of ϕ at the interface ($x = 0$)

$$\partial_x\phi\big|_{x=0}=\frac{\phi_b^2\sqrt{1-\psi_b}}{\sqrt{2}\mathrm{Cn}}=\frac{\sqrt{1-\psi_b}}{\sqrt{2}\mathrm{Cn}}\left(1-\frac{\psi_b}{\mathrm{Ex}\left(1-\psi_b\right)}\right)<\frac{1}{\sqrt{2}\mathrm{Cn}} \tag{3.8}$$

It can be observed from (3.8) that the introduction of surfactants increases the interface thickness, which is determined by the Cahn number Cn, the surfactant bulk concentration ψ_b and the parameter Ex. The decrease in Ex or increase in ψ_b will further decrease the gradient of ϕ on the interface, leading to a more diffuse interface. Since the surfactant bulk concentration ψ_b is far small than unity ($\psi_b << 1$), the variation of the interface thickness is small even at the high surfactant bulk concentration. Thus, to some extent, it is reasonable to assume that the interface thickness is unchanged when we analytically derive some equilibrium properties of surfactant adsorption, especially at the low surfactant bulk concentration. This simplification will greatly facilitate our derivations. Then (3.8) can be reduced to

$$\partial_x\phi\big|_{x=0}=1\Big/\left(\sqrt{2}\mathrm{Cn}\right). \tag{3.9}$$

Now we analyze the equilibrium properties of surfactant adsorption (Engblom et al. 2013; Liu & Zhang 2010). The chemical potential w_ψ at any position can be written as

$$w_\psi=\mathrm{Pi}\ln\left(\frac{\psi}{1-\psi}\right)+\frac{1}{2\mathrm{Ex}}\phi^2-\frac{\left(\phi^2-1\right)^2}{4}, \tag{3.10}$$

and w_ψ in the pure phases reads:

$$w_{\psi_b}=\mathrm{Pi}\ln\left(\frac{\psi_b}{1-\psi_b}\right)+\frac{1}{2\mathrm{Ex}}\phi_b^2-\frac{\left(\phi_b^2-1\right)^2}{4}. \tag{3.11}$$

Since w_ψ is constant in equilibrium, subtracting (3.11) from (3.10), and introducing the intermediate variable ψ_c, we get the relation

$$\mathrm{Pi}\ln\psi_c=-\frac{1}{2\mathrm{Ex}}\left(\phi_b^2-\phi^2\right)-\frac{1}{4}\left[\left(\phi^2-\phi_b^2\right)\left(\phi_b^2+\phi^2-2\right)\right], \tag{3.12}$$

then the equilibrium profile for ψ can be obtained

$$\psi=\frac{\psi_b}{\psi_b+\psi_c\left(1-\psi_b\right)}. \tag{3.13}$$

Considering the fact that ϕ=0 on the interface of fluids, phase bulk value $\phi_b = \pm 1$ and $\psi_b << 1$, (3.13) and (3.12) can be simplified as

$$\psi_0=\frac{\psi_b}{\psi_b+\psi_c}, \tag{3.14}$$

$$\mathrm{Pi}\ln\psi_c=-\frac{1}{4}\left(1+\frac{2}{\mathrm{Ex}}\right), \tag{3.15}$$

where ψ_0 is the equilibrium surfactant concentration on the interface. The equation (3.14) is the typical Langmuir isotherm and the intermediate variable ψ_c can be viewed as the Langmuir adsorption constant. Given specific Pi (temperature-dependent constant) and ψ_c, the parameter Ex can be obtained from (3.15). The adsorption isotherm is important for the following simulations.

Shape interface models simulate the interfacial flows with surfactants using an equilibrium equation of state, which relates the dynamic interfacial tension to the surfactant concentration on the interface, and the equilibrium equation of state can be derived by integration of the Gibbs

equation $d\sigma = -\psi_0 dw_{\psi,0}$ (isothermal system), where $w_{\psi,0}$ is the chemical potential on the interface. However, for the phase-field model, the excess amount of surfactants has to be obtained via integration over the whole diffuse interface, and thus there exists no analytical solution for the equilibrium equation of state. Following the idea in Van der Sman and Van der Graaf (2006), we assume that the excess amount of surfactants is proportional to ψ_0, so that the interfacial lowering $d\sigma$ is proportional to that of the sharp interface with a coefficient k, i.e.,

$$d\sigma = -k\psi_0 dw_{\psi,0}. \tag{3.16}$$

where the coefficient k should be independent of ψ_0. We know that $k = 1$ for the sharp interface model, while $k \neq 1$ for the diffuse interface model due to the finite interface thickness. As we mentioned above, k depends on the excess amount of surfactants. Considering the fact that the Langmuir isotherm determines the equilibrium profile of surfactants (diffuse interface), we can infer from (3.14) and (3.15) that, for the given Langmuir adsorption constant ψ_c, the excess surfactant concentration is a function of the interfacial thickness Cn, ψ_0 and Ex (Pi can be determined by Ex and ψ_c). As k is independent of ψ_0, k only depends on Ex once the interfacial thickness Cn is specified.

Substituting (3.10) into (3.16), and integrating on both sides of (3.16), we obtain the equation of state

$$\Delta\sigma = \sigma - \sigma_0 = k\mathrm{Pi}\ln\left(1-\psi_0\right). \tag{3.17}$$

The equation (3.17) will be validated in Section 4.1.

4. Numerical results

In this section, we first use the classical droplet spread case to validate the MCL model and the analytically derived equilibrium properties. Then we investigate the droplet dynamics with soluble surfactants on a chemically patterned surface.

4.1. Numerical validation

Most previous studies on two-phase flows with the MCL utilized sharp interface models with an equilibrium equation of state, and their models only considered insoluble surfactants on the interface, which were quite different from the diffuse interface model with soluble surfactants in this study. Thus, it is difficult to find an appropriate benchmark to validate our model. If the surfactant concentration is set to 0 (clean droplet), then the derived model reduces to the phase-field MCL model, which can be easily validated. We first use a classical benchmark to verify the phase-field MCL model, as shown in Figure 1. The rectangular computational domain Ω is set as $[0, 1] \times [0, 2]$, and periodic boundary conditions are applied in the horizontal direction. Initially, a semicircular droplet with the radius $R_0 = 0.5$ and the contact angle $\theta_0 = 90^o$ is placed on the bottom surface (Figure 1a). The gravitational effect is neglected in this case. The Reynolds number Re, the capillary number Ca, and the Péclet number Pe_ϕ are taken as 10, 0.1 and 10, respectively. The Cahn number Cn, measuring the thickness of diffuse interface, is 0.01. The relaxation parameter Pe_s and slip length L_s are set to 0.005 and 0.0038, respectively. Both density ratio λ_ρ and viscosity ratio λ_ν of the droplet to the surrounding fluid are 1.1. We use a grid size of 300×150 and time step size $\delta t = 2.5\times10^{-4}$ in all simulations.

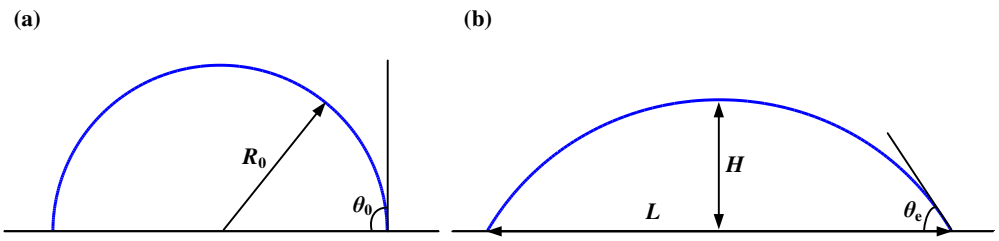

Figure 1. Illustration of (a) initial shape of the droplet with the radius of R_0 released on the bottom surface and (b) equilibrium shape of the droplet. The size of computational domain is $[0, L_x] \times [0, L_y]$. In (a), the droplet center is located at $(L_x/2, 0)$. In (b), L is the spreading length and H is the droplet height. The gravitational effect is neglected in this case. θ_0 is the initial contact angle and θ_e is the equilibrium contact angle. Note that θ_e is equal to the static contact angle θ_s for the clean droplet.

The droplet driven by the unbalanced Young stress will spread or recoil to the equilibrium shape with the prescribed static contact angle θ_s (θ_s is equal to the equilibrium contact angle θ_e for the clean droplet). In equilibrium, the spreading length L and droplet height H in Figure 1(b) can be analytically obtained by the law of mass conservation (Cai et al. 2014)

$$L = 2R_0\sqrt{\frac{\pi}{2\left(\theta_s - \sin\theta_s\cos\theta_s\right)}}\sin\theta_s, \quad H = R_0\sqrt{\frac{\pi}{2\left(\theta_s - \sin\theta_s\cos\theta_s\right)}}\left(1-\cos\theta_s\right). \tag{4.1}$$

We conduct several simulations in a wide range of surface wettability for both hydrophilic and hydrophobic cases (θ_s varies from 45º to 135º). Analytical and numerical values of L and H are compared in Figure 2, and a good agreement is observed for all values of θ_s.

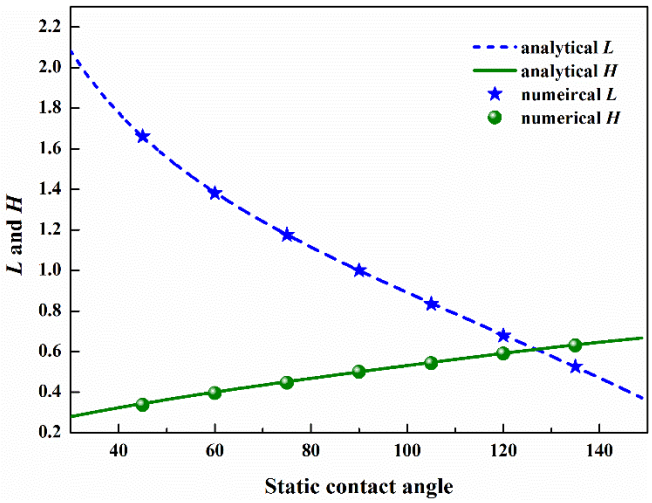

Figure 2. The comparison of analytical and numerical values of spreading length L and droplet height H at different static contact angles θ_s. θ_s ranges from 45º to 135º with an interval 15º.

To clearly demonstrate the effect of surfactants on the MCL, we compare the dynamics of clean and contaminated (with surfactants) droplets. The Langmuir adsorption constant ψ_c and the parameter Ex take 0.017 and 1, respectively, with the value of Pi determined from (3.15). Other parameters are taken as before. Both hydrophilic (θ_s = 60º) and hydrophobic (θ_s = 120º) cases are considered in this study. For the contaminated droplet, the initialization of surfactant concentration is performed using the analytical prediction in equation (3.14) for ψ with the initial surfactant bulk concentration $\psi_b = 1.5\times10^{-2}$.

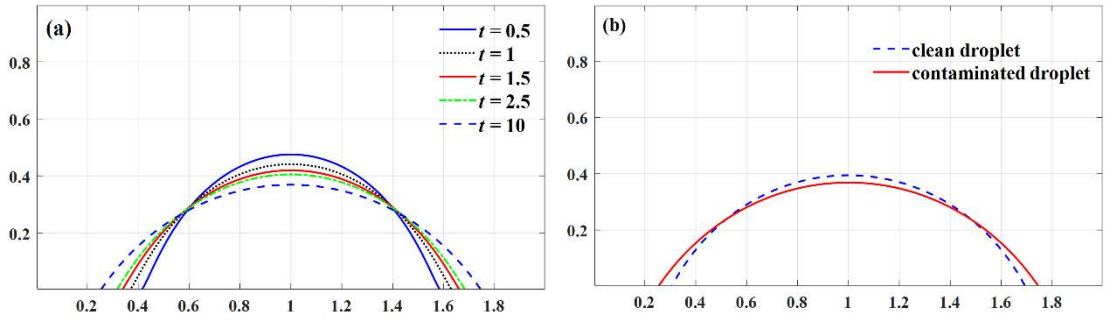

Figure 3. Profiles of (a) the contaminated droplet at different times and (b) clean and condaminated droplets in equilibrium on a hydrophilic surface with the static contact angle θ_s = 60º. For the contaminated droplet, the initial surfactant bulk concentration ψ_b is 1.5×10^{-2}. In (b), equilibrium contact angles θ_e for clean and contaminated droplets are 60º and 52º, respectively.

Figure 3(a) gives the evolution of contaminated droplet on a hydrophilic surface at different times (t ranges from 0 to 10). The contaminated droplet constantly spreads until the steady state reaches. Equilibrium contact angles θ_e for clean and contaminated droplets in Figure 3(b) are 60º and 52º, respectively. Obviously, the presence of surfactants makes the droplet more hydrophilic on a hydrophilic surface. In contrast to the hydrophilic surface, surfactants make the droplet more hydrophobic on a hydrophobic surface by increasing the equilibrium contact angle θ_e from 120º to 129º, as shown in Figure 4. Results in Figure 3 and Figure 4 are consistent with the results obtained by sharp interface models (Lai et al. 2010; Xu & Ren 2014; Zhang et al. 2014). We further calculate the spreading length L, the droplet height H and θ_e for the contaminated droplet ($\psi_b = 1.5\times10^{-2}$) in a wide range of surface wettability (θ_s varies from 45º to 135º). Analytical L and H for the clean droplet in Figure 5 serve as a comparison. It is observed from Figure 5 that the effect of surfactants is more obvious on the strong hydrophilic or hydrophobic surface. The inset gives θ_e of the contaminated droplet. The blue line in the inset represents static contact angles θ_s of the clean droplet (the slop of this line is 1), and it serves as a reference. We found that θ_e can be approximately predicted by θ_s through a linear relationship $\theta_e = 1.3\theta_s - 25.7$.

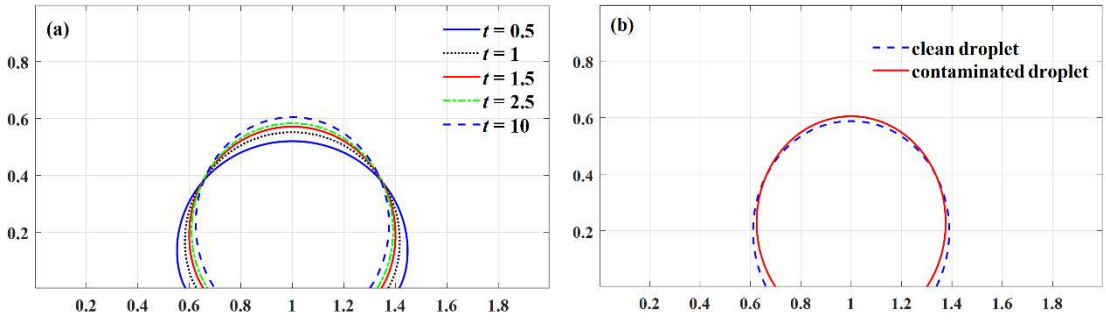

Figure 4. Profiles of (a) the contaminated droplet at different times and (b) clean and condaminated droplets in equilibrium on a hydrophobic surface with the static contact angle θ_s = 120º. For the contaminated droplet, the initial surfactant bulk concentration ψ_b is 1.5×10^{-2}. In (b), equilibrium contact angles for clean and contaminated droplets are 120º and 129º, respectively.

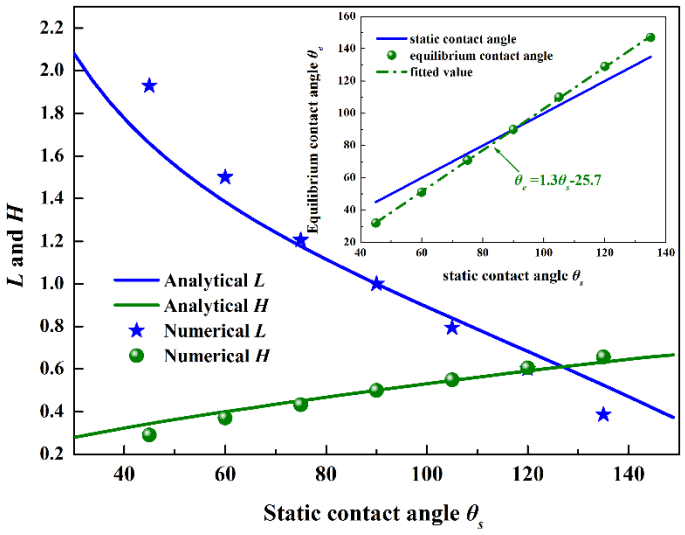

Figure 5. Numerical spreading length L (points) and droplet height H (points) for the contaminated droplet, and analytical values (lines) calculated from static contact angles serve as a compression. For the contaminated droplet, the initial surfactant bulk concentration ψ_b is 1.5×10^{-2}. The inset gives θ_e of contaminated droplet. It can be observed that θ_e can be approximately predicted by θ_s through a linear relationship $\theta_e = 1.3\theta_s - 25.7$.

We also extend our work to a three-dimensional (3D) computational domain $[0, 0.8]^2 \times [0, 0.4]$. A grid size of $110^2 \times 55$ and time step size $\delta t = 8\times10^{-4}$ are used in simulations. For the contaminated droplet, the initial surfactant bulk concentration ψ_b is 2.5×10^{-2}. Results in Figure 6 clearly demonstrate the effect of surfactants on the contact line dynamics. The presence of surfactants reduces θ_e from 60º to 42º on the hydrophilic surface, and increases θ_e from 120º to 139º on the hydrophobic surface.

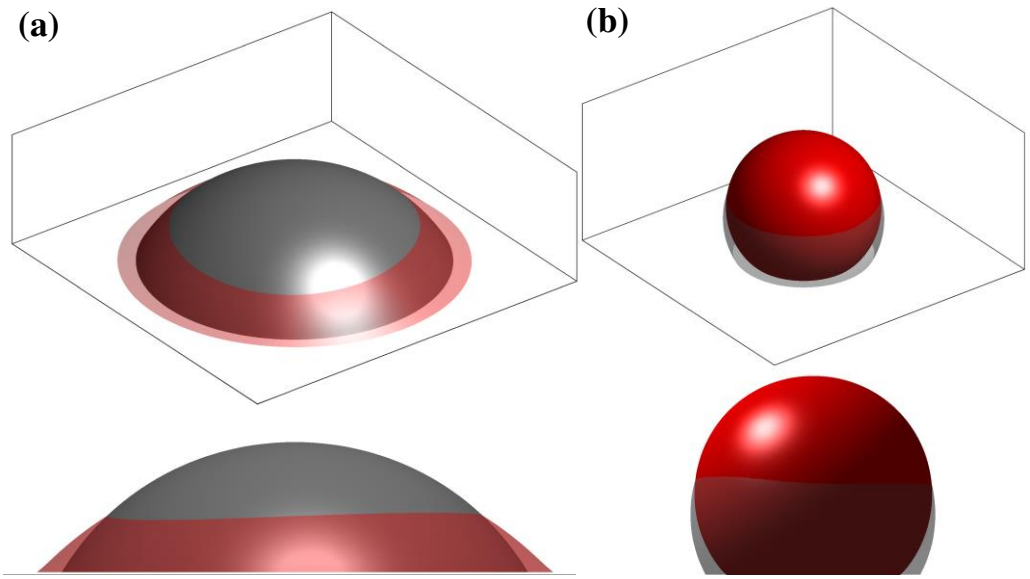

Figure 6. Profiles of clean and contaminated droplets on hydrophilic ($\theta_s = 60º$) and hydrophobic ($\theta_s = 120º$) surfaces. For the contaminated droplet, the initial surfactant bulk concentration ψ_b is 2.5×10^{-2}. The computation domain is $[0, 0.8]^2 \times [0, 0.4]$. We use a grid size of $110^2 \times 55$ and time step size $\delta t = 8\times10^{-4}$ in simulations. In (a), equilibrium contact angles θ_e of clean and contaminated droplets are 60º and 42º, respectively. In (b), equilibrium contact angles

θ_e of clean and contaminated droplets are 120° and 139°, respectively.

The Young's equation can well explain the effect of surfactants on the droplet dynamics on the solid surface. As in Wang et al. (2008), we can derive that

$$\int_{int}[L\partial_\tau\phi]\mathrm{d}\tau=\int_{int}\left[\mathrm{Cn}\partial_n\phi\partial_\tau\phi+M'(\phi)\partial_\tau\phi\right]\mathrm{d}\tau=\sigma_e\cos\theta_e+\Delta\sigma_{fs}, \tag{4.2}$$

where $\int_{int}\mathrm{d}\tau$ denotes the integration across the fluid-fluid interface along the τ-direction, $\Delta\sigma_{fs}$ is a function of the local composition at the solid surface measuring the fluid-solid interfacial free energy per unit area, and σ_e is the interfacial tension of contaminated droplet in equilibrium. The equation (4.2) indicates that the unbalanced Young stress dominates the evolution of contact angle. It drives the droplet at two contact points to spread on a hydrophilic surface or to recoil on a hydrophobic surface. In equilibrium, the unbalanced Young stress decreases to zero (Figure 7), namely $L = 0$, and (4.2) reduces to the classical Young's equation

$$\sigma_e\cos\theta_e+\Delta\sigma_{fs}=0. \tag{4.3}$$

The boundary condition $\partial_n\psi=0$ allows the presence of free surfactants on the fluid-solid interface, but these surfactants do not affect the fluid-solid interfacial tension through the adsorption or the like, so clean and contaminated droplets have the same $\Delta\sigma_{fs}$. Then we have

$$\sigma_e\cos\theta_e=\sigma_0\cos\theta_s, \tag{4.4}$$

where σ_0 is the interfacial tension of a clean droplet. The addition of surfactants greatly reduces the interfacial tension between fluids, resulting in $\sigma_e < \sigma_0$. We can derive that $\cos\theta_e > \cos\theta_s$ from (4.4). Thus, θ_e is smaller than θ_s in the hydrophilic case (the contaminated droplet becomes more hydrophilic), and θ_e is larger than θ_s in the hydrophobic case (the contaminated droplet becomes more hydrophobic).

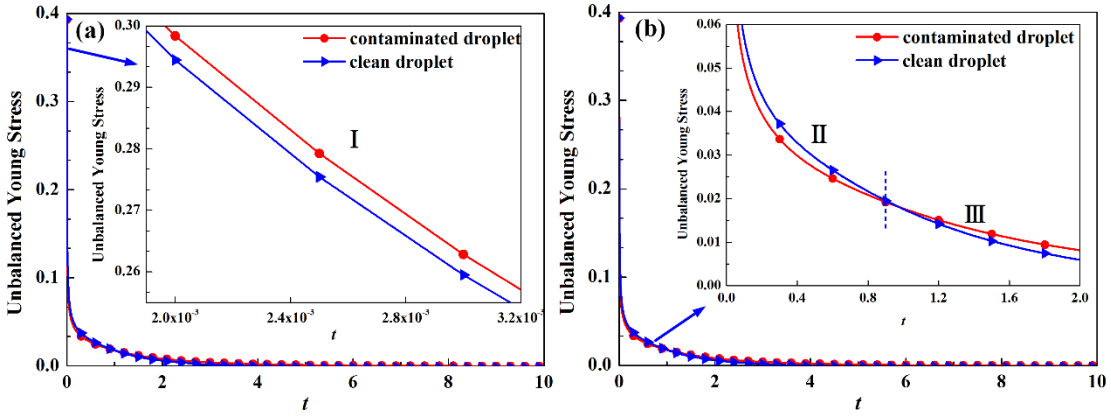

Figure 7. Evolutions of unbalanced Young stresses at right contact points of clean and contaminated droplets (ψ_b = 1.5×10^{-2}). The static contact angle θ_s of the hydrophilic surface 60°.

We denote the unbalanced Young stresses at right contact points of clean and contaminated droplets as F_{Rc} and F_{Rs}, respectively. Figure 7 gives evolutions of F_{Rc} and F_{Rs}, and the whole process

can be divided into three stages. At the first stage, the contaminated droplet spreads faster than the clean droplet since F_{Rs} is larger than F_{Rc}. During the droplet spreading process, the unbalanced Young stress always drags the right contact point forward to reduce the contact angle, and it decreases as the contact angle changes until equilibrium. Thus, to some extent, the unbalanced Young stress can be reflected on the contact angle. Obviously, at the same moment, the contaminated droplet has a smaller contact angle than the clean droplet, which explains why the change in F_{Rs} is more dramatic in the second stage. It can be observed that F_{Rs} is larger than F_{Rc} in the third stage, and this fact may account for a smaller equilibrium contact angle of the contaminated droplet.

The interfacial tension lowering $\Delta\sigma$ of contaminated droplet in equilibrium can be calculated from (4.5)

$$\Delta\sigma = \sigma_e - \sigma_0 = \sigma_0\left(\frac{\cos\theta_s - \cos\theta_e}{\cos\theta_e}\right). \tag{4.5}$$

Now we perform a series of numerical experiments to verify the linear relationship between $\Delta\sigma$ and $\ln(1-\psi_0)$ analytically obtained in equation (3.17). Two different scenarios are considered in this study: Ex = 0.5 and Ex =1. In each scenario, we conduct simulations with different surfactant bulk concentrations, e.g., $\psi_b = 1\times10^{-2}$, 1.5×10^{-2} and 2×10^{-2}. The static contact angle θ_s of bottom surface is taken to be 60º. From the resulting profile of surfactant concentration in equilibrium, the surfactant loading of interface ψ_0 can be directly obtained. The equilibrium contact angle θ_e can be easily calculated when the contaminated droplet reaches the steady state, and then we get the interfacial tension lowering $\Delta\sigma$ from equation (4.5). Obviously, there is a linear relationship between $\Delta\sigma$ and $\ln(1-\psi_0)$, as plotted in Figure 8, which directly validates the equilibrium equation of state (3.17). We use linear formulas to fit simulated values at different Ex, and fitted equations of green and blue lines can be approximated as $\Delta\sigma/\sigma_0 = 0.3396\ln(1-\psi_0)$ and $\Delta\sigma/\sigma_0 = 0.1942\ln(1-\psi_0)$, respectively. It worth noting that, Ex plays an important role in reducing the interfacial tension, and its effect is more obvious at the higher interfacial surfactant concentration. we infer, in the last part of Section 3, that the coefficient k is determined by Ex for the given Langmuir adsorption constant ψ_c and the interfacial thickness Cn. It can be observed that the slopes (kPi) of two fitted curves in Figure 8 equals 0.1942 (Ex=1) and 0.3396 (Ex=0.5), respectively. The dimensionless parameter Pi can be calculated from (3.15). Then we can obtain that k equals 1.05 and 1.11 for the cases of Ex = 1 and Ex = 0.5, respectively. This result has verified our inference that k depends on Ex.

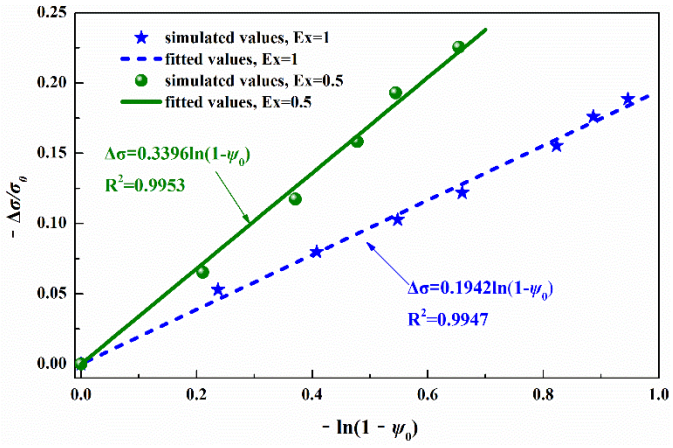

Figure 8. The linear relationship between the interfacial tension lowering $\Delta\sigma/\sigma_0$ and $\ln(1-\psi_0)$. Fitted formulas of green and blue lines can be approximated as $\Delta\sigma/\sigma_0 = 0.3396\ln(1-\psi_0)$ and $\Delta\sigma/\sigma_0 = 0.1942\ln(1-\psi_0)$, respectively.

Results in Figure 8 directly validates the equilibrium equation of state (3.17).

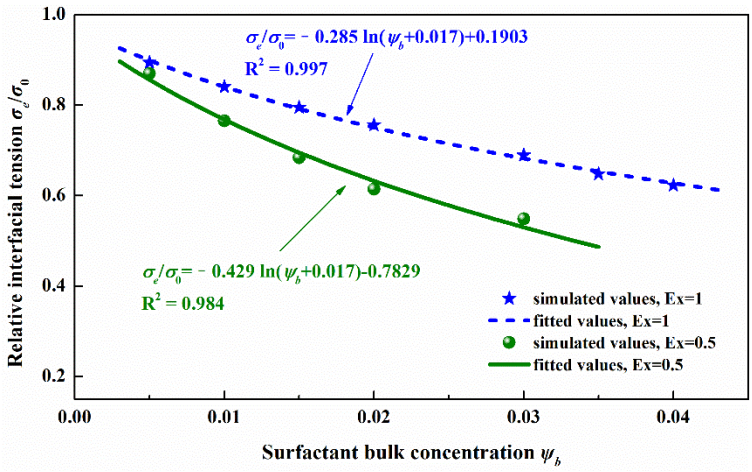

Figure 9. The relative interfacial tension σ_e/σ_0 at different surfactant bulk concentrations ψ_b. The Langmuir adsorption constant ψ_c is 0.017. The analytical equation (4.6) fits simulated values very well.

Using the Langmuir isotherm in equation (3.14) and equilibrium equation of state (3.17), we obtain the relationship between the relative interfacial tension σ_e/σ_0 and surfactant bulk concentration ψ_b,

$$\sigma_e/\sigma_0 = -\frac{k\,\mathrm{Pi}}{\sigma_0}\ln\left(\psi_b+\psi_c\right)+\frac{k\,\mathrm{Pi}}{\sigma_0}\ln\psi_c+1, \tag{4.6}$$

where the Langmuir adsorption constant ψ_c is 0.017 in this study. It can be observed that equation (4.6) fits simulated values very well in Figure 9, indicating that the correctness of the Langmuir isotherm and the equilibrium equation of state to some extent. Again, we can see that the coefficient k is determined by Ex.

4.2. Droplet dynamics on a chemically patterned surface

4.2.1. Phase diagram of flow states

Having validated the MCL model, we investigate the droplet dynamics with soluble surfactants on a chemically patterned surface. The computational domain is $\Omega = [0, 4] \times [0, 1]$ with periodic boundary conditions applied on the horizontal direction, as shown in Figure 10. Initially, a semicircular droplet with the radius of 0.5 is placed on the bottom surface with static contact angles θ_1 ($\theta_1 < 90^o$) for the hydrophilic A-type stripe and θ_2 ($\theta_2 > 90^o$) for the hydrophobic B-type stripe, respectively. The droplet center locates at (1, 0). A constant body force along the horizontal direction is applied on the droplet. A grid size of 600×150 and time step size $\delta t = 5\times10^{-4}$ are used in all simulations. The Reynolds number Re, Péclet numbers Pe_ϕ and Pe_ψ are taken as 20, 100 and 10, respectively. The value of Cahn number Cn is 0.01. The relaxation parameter Pe_s and slip length L_s are set to 0.005 and 0.0038, respectively. Both density ratio λ_ρ and viscosity ratio λ_ν of the droplet to the surrounding fluid are 2. The initial surfactant bulk concentration ψ_b is 1.5×10^{-2}. To clearly demonstrate the effect of surfactants, we compare the dynamics of clean and contaminated droplets.

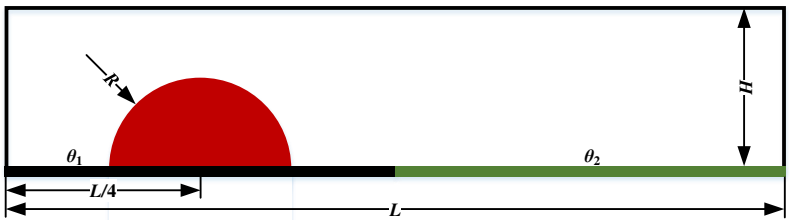

Figure 10. Schematic of computation domain $\Omega = [0, L] \times [0, H]$. A semicircular droplet with the radius of $L/8$ is placed on a chemically patterned surface with static contact angles θ_1 ($\theta_1 < 90^o$) for the hydrophilic A-type stripe (black stripe) and θ_2 ($\theta_2 > 90^o$) for the hydrophobic B-type stripe (green stripe), respectively. The droplet center locates at ($L/4$, 0). The droplet is pushed along the horizontal direction by a constant body force.

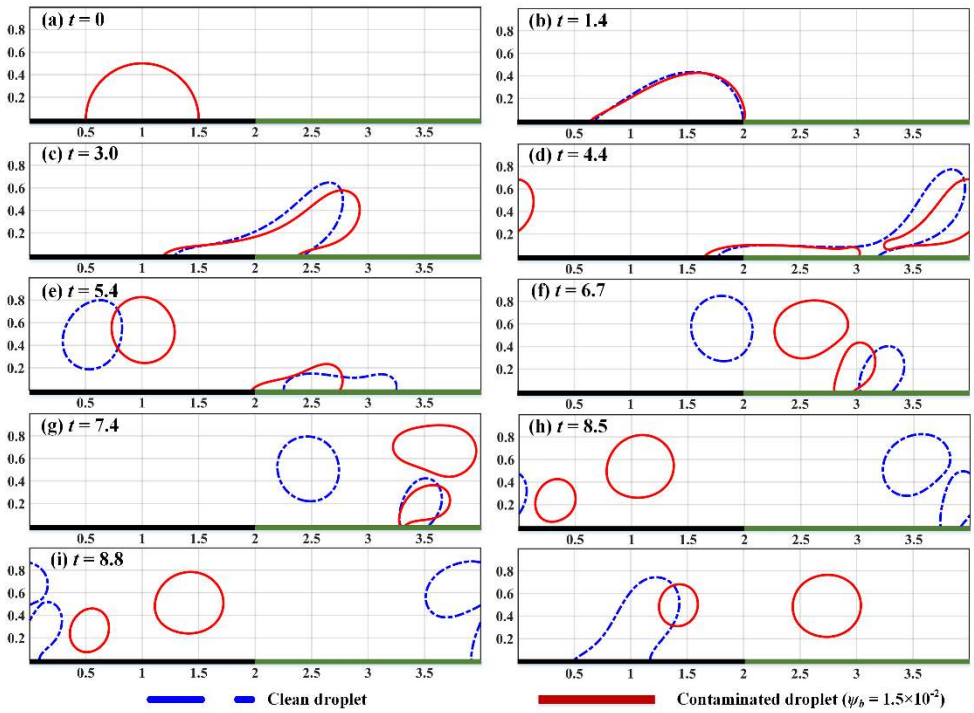

Figure 11. Dynamics of clean (blue) and contaminated (red) droplets on a chemically patterned surface with static contact angles $\theta_1 = 60^o$ for the A-type stripe (black stripe) and $\theta_2 = 120^o$ for the B-type stripe (green stripe). Droplets are pushed by a constant body force along the horizontal direction.

Figure 11 gives the evolution of droplets on a chemically patterned surface. At first, both clean and contaminated droplets spread out over the hydrophilic surface due to the unbalanced Young stress, and then move forward under the action of a constant body force (Figure 11b). After crossing the junction of wettability transition, both droplets suffer from large deformation and break up into daughter droplets. Obviously, compared with the clean droplet, the contaminated droplet has a larger advancing angle on the hydrophobic B-type stripe and a smaller receding angle on the hydrophilic A-type stripe (Figure 11c). We also note that the breakup of the contaminated droplet occurs earlier than the clean droplet (Figure 11d). After the breakup, the spreading droplets left on the hydrophobic stripe begin to contract (Figure 11e). Subsequently, daughter droplets detached from the solid surface move towards daughter droplets in contact with the B-type stripe (Figure 11f). As two clean daughter droplets approach each other, the film between them becomes very thin, and then they

merge together due to the effect of interfacial tension. The merging droplet continues to slide on the hydrophilic A-type stripe (Figure 11j). While the thin film between two contaminated daughter droplets is always maintained at a certain thickness until they slide over each other (Figure 11h). Note that both contaminated daughter droplets eventually detach from the bottom surface. Figure 12 shows the evolution of surfactant concentration. The surfactant concentration around the interface is much larger than other region, and the distribution of surfactants is non-uniform along the interface. In fact, the different behavior between contaminated and clean droplets is caused by (1) the uniform reduction of interfacial tension, and (2) the non-uniform effects from the non-uniform interfacial tension and the Marangoni stress along the interface. We also see that surfactants are swept into the bulk phases when concentration reaches the maximum at the droplet tip (Figure 12e). Figure 13 presents the evolutions of pressure field and surfactant concentration during the collision of two contaminated droplets. It can be observed that the pressure in the gap between two contaminated droplets increases significantly as they approach each other (point A to point C). The increasing pressure pushes surfactants away from the near-contact region, and the resulting Marangoni force acts as a repulsive force to prevent droplet coalescence (Liu & Zhang 2010; Wodlei et al. 2018). The pressure in the gap decreases (point D to point E) as two contaminated droplets slide over each other.

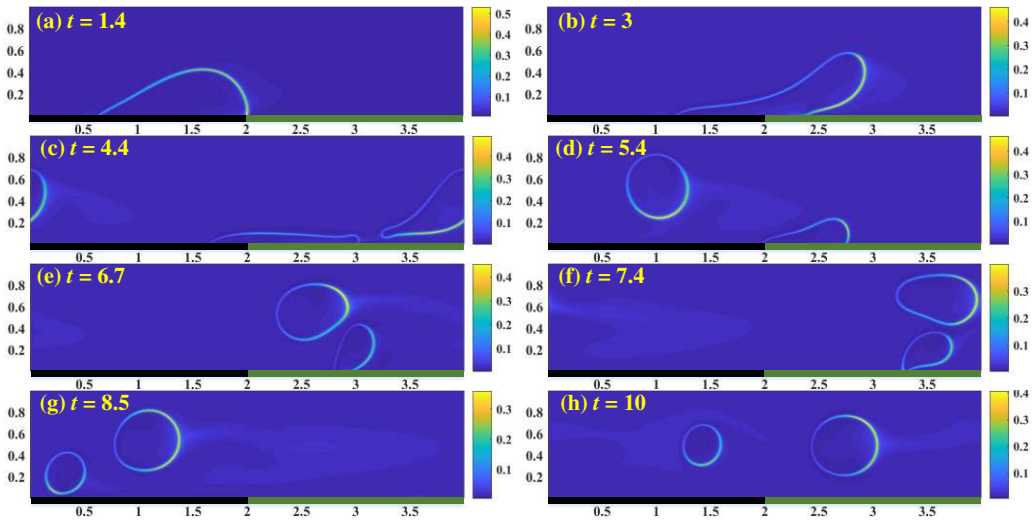

Figure 12. Evolution of the surfactant concentration for the contaminated droplet. The initial surfactant bulk concentration ψ_b is 1.5×10^{-2}.

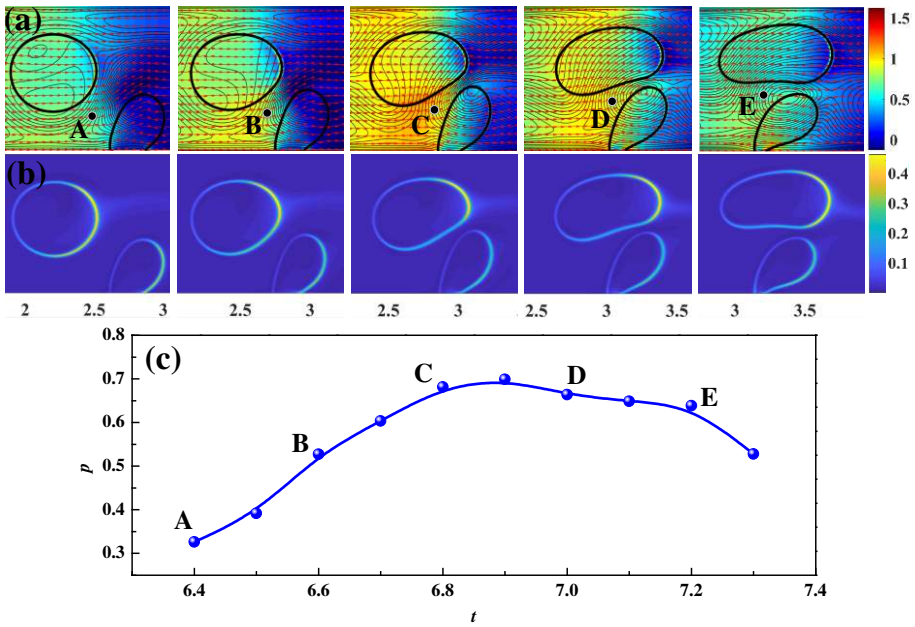

Figure 13. Evolutions of (a) pressure field (background color), (b) surfactant concentration and (c) pressure during the separation of two contaminated droplets. The initial surfactant bulk concentration ψ_b is 1.5×10^{-2}.

There are several parameters that potentially influence the dynamics of a contaminated droplet on a chemically patterned surface, e.g., the surfactant bulk concentration ψ_b, the defect strength $\Delta\theta_e = \theta_2 - \theta_1$, the Reynolds number Re, etc. In this work, we only consider the effect of ψ_b and $\Delta\theta_e$ on the behavior of a contaminated droplet. A series of numerical simulations, with ψ_b ranging from 1×10^{-3} to 1.5×10^{-2} and $\Delta\theta_e$ ranging from 20º to 100º, are conducted to obtain a clear understanding of the droplet dynamics. Other parameters and boundary conditions remain unchanged. Results demonstrate that all contaminated droplets at various conditions suffer from the large deformation and breakup, just like Figure 11 (c) and (d). After the droplet breakup, we observe three typical flow states, specifically, the coalescence mode, the non-coalescence mode and the detachment mode, as shown in Figure 14. At the low ψ_b and medium $\Delta\theta_e$ ($\psi_b = 1\times10^{-3}$ and $\Delta\theta_e = 70$º), the coalescence occurs as two contaminated droplets move towards each other because of the interfacial tension. At the high ψ_b and low $\Delta\theta_e$ ($\psi_b = 1.5\times10^{-2}$ and $\Delta\theta_e = 50$º), the repulsive Marangoni force together with the low interfacial tension leads to the separation of two daughter droplets, and the droplet in contact with the bottom wall will continue to slide on the hydrophilic A-type stripe. This phenomenon is called "non-coalescence". If we increase $\Delta\theta_e$ on the basis of the non-coalescence event ($\psi_b = 1.5\times10^{-2}$ and $\Delta\theta_e = 70$º), the detachment event will occur, when the droplet sliding on the bottom wall (green stripe) leaves the patterned surface. Note that the droplet can only detach from the solid surface on the hydrophobic B-type stripe (green stripe).

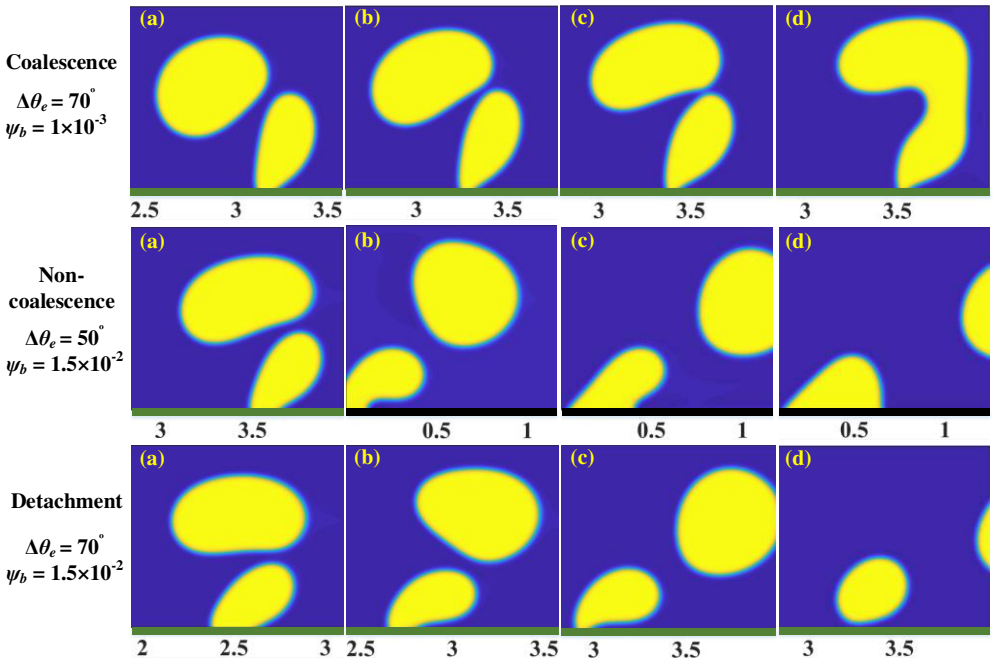

Figure 14. Three typical flow states of contaminated droplets at various surfactant bulk concenrtations ψ_b and defect strengths $\Delta\theta_e$: the coalescence, the non-coalescence and the detachment. A-type stripe (black stripe) with the static contact angle θ_1 is hydrophilic and B-type stripe (green stripe) with the static contact angle θ_2 is hydrophobic. We define the defect stength $\Delta\theta_e$ as the difference of θ_1 and θ_2, namely, $\Delta\theta_e = \theta_2 - \theta_1$.

A phase diagram of flow states for contaminated droplets at different ψ_b and $\Delta\theta_e$ is further reported in Figure 15. A black star identifies a coalescence event, a red diamond marks a non-coalescence event and a blue circle represents a detachment event. As we can see, only the non-coalescence occurs for all ψ_b when $\Delta\theta_e$ is less than 60º. The surfactant bulk concentration ψ_b begins to affect the flow state of droplet as the defect strength $\Delta\theta_e$ increases to 60º. Detachment events occur at the high ψ_b since surfactants reduce the adsorption effect of B-type stripe by increasing advancing contact angles of droplets. With the decrease of ψ_b, droplets cannot detach from the B-type stripe due to the weak effect of surfactants, and non-coalescence phenomena appear. If we further reduce ψ_b, a large interfacial tension will lead to the coalescence of two contaminated droplets. It can be observed that non-coalescence events occur on a narrower range of ψ_b at $\Delta\theta_e$ = 70º and completely disappear when $\Delta\theta_e$ is larger than 70º. Detachment and coalescence events dominate flow states of droplets at $\Delta\theta_e$ = 80º. Coalescence events only occur at specific surfactant bulk concentrations when $\Delta\theta_e$ is larger than 80º. Overall, the non-coalescence event is the only flow state of contaminated droplets at the low defect strength ($\Delta\theta_e \leq$ 50º) and completely disappears at the high defect strength ($\Delta\theta_e \geq$ 80º). All three flow states occur at the medium defect strength (50º < $\Delta\theta_e$ < 80º). The detachment event dominates the flow behavior of droplets at the high defect strength.

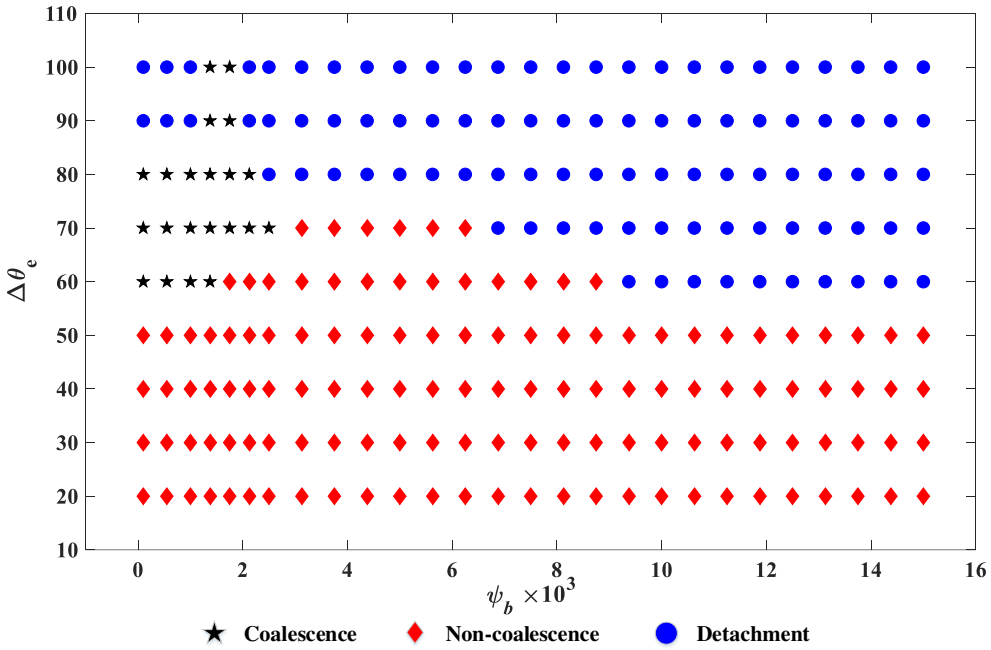

Figure 15. A phase diagram of flow states for contaminated droplets at different surfactant bulk concentrations ψ_b and defect strengths $\Delta\theta_e$. A black star identifies a coalescence event, a red diamond marks a non-coalescence event and a blue circle represents a detachment event.

4.2.2. Unbalanced Young stress at the moving contact line

In this section, we focus on the evolution of the unbalanced Young stress $L\partial_\tau\phi$ when a contaminated droplet moves across the junction of wettability transition. As a contaminated droplet moves along the x direction, the advancing contact angle and receding contact angle are denoted as θ_A and θ_R, respectively. F_A and F_R are unbalanced Young stresses acting on the triple-phase contact points A and R, respectively. As shown in Figure 16, the unbalanced Young stress is defined as positive when it points from left to right, otherwise, it is defined as negative. We calculate unbalanced Young stresses F_A and F_R within the time range of 0 to 2.8, and details of droplet dynamics in this period can refer to Figure 11 (a) - (c). During the process, the triple-phase contact point A moves from the hydrophilic A-type stripe to the hydrophobic B-type stripe, while the point R never crosses the junction.

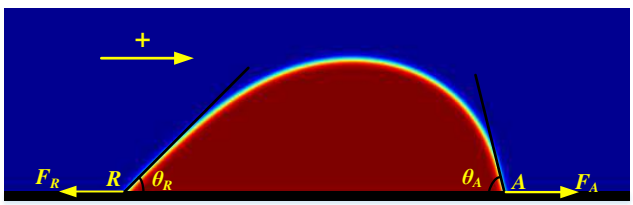

Figure 16. Illustration of unbalanced Young stresses F_A and F_R at the triple-phase contact points A and R. θ_A is the advancing contact angle and θ_R is the receding contact angle.

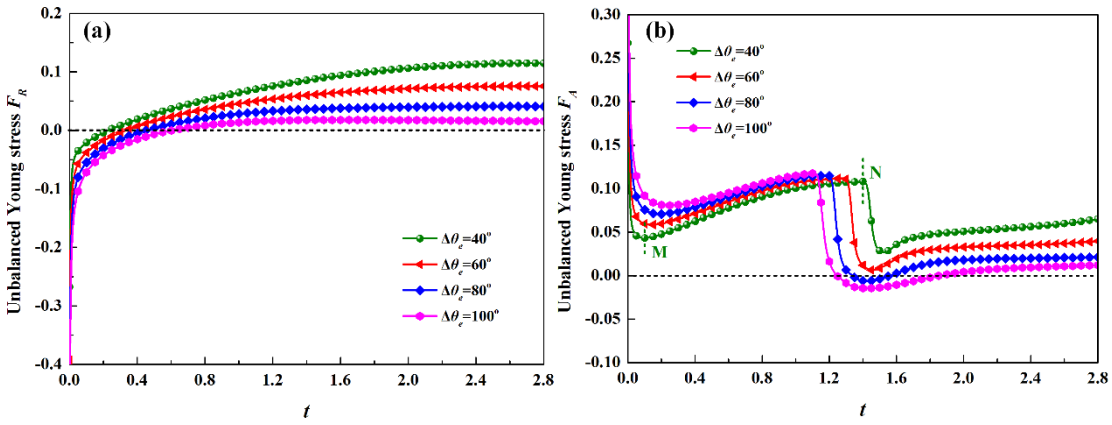

Figure 17. Evolutions of unbalanced Young stresses F_R and F_A at different defect strengths $\Delta\theta_e$. The initial surfactant bulk concentration ψ_b is 1.5×10^{-2}.

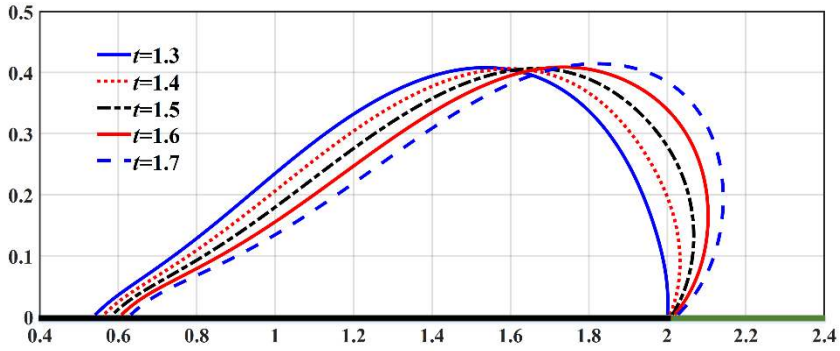

Figure 18. profiles of phase-field variable ϕ at different times. The initial surfactant bulk concentration ψ_b is 1.5×10^{-2}.

The chemical potential L in the unbalanced Young stress measures the deviation from the equilibrium condition ($L = 0$) at the solid surface, and the main role of the unbalanced Young stress is to adjust the droplet to its equilibrium condition (equilibrium contact angle θ_e). Figure 17 gives the evolutions of unbalanced Young stresses F_R and F_A. Initially, the static droplet ($\theta_0 = 90^o$) spreads on the hydrophilic surface under the action of F_R and F_A. F_R points to the left (negative) and F_A points to the opposite direction (positive). Both F_R and F_A decrease dramatically as θ_R and θ_A approach the equilibrium contact angle θ_e ($\theta_e < \theta_s$ on a hydrophilic surface). Meanwhile, the droplet keeps deforming as a constant body force drives it forward. The receding contact angle θ_R decreases with the deformation of droplet, and F_R becomes zero when θ_R decreases to θ_e, as shown in Figure 17(a). The continuous deformation of droplet causes the receding contact angle θ_R to continue to decrease ($\theta_R < \theta_e$). In order to adjust the contact point R to the equilibrium condition, F_R changes its direction (now it points to the right, positive) and pushes the contact point R to move forward. During the whole process, the contact point R never moves across the junction of wettability transition.

The evolution of F_A is more complicated than F_R. Before θ_A decreases to the equilibrium contact angle θ_e, the droplet deformation leads to the increase of θ_A, which is contrary to the expectation of F_A. Thus, F_A begins to increase (point M in Figure 17b) and drags the contact point A forward to reduce θ_A. As the contact point A meets the junction, F_A experiences a dramatic

decrease (point N). According to the GNBC, the drop of F_A must be accompanied by the decrease of fraction force due to the contact line slip. Thus, the classical phenomenon that contact line sticking to the solid surface is expected to occur at the point N, and this is actually observed in Figure 18.

In Figure 17(b), we can see that the defect strength $\Delta\theta_e$ has a significant impact on the behavior of F_A. When the defect strength $\Delta\theta_e$ is less than 80º, θ_A immediately arrives at the equilibrium contact angle θ_e of the hydrophobic B-type stripe. With the droplet deformation, θ_A continues to increase and exceeds θ_e, and correspondingly, F_A rises to reduce θ_A. Throughout the whole process, F_A never changes direction, and always drags the contact point A forward. The behavior of F_A becomes complicated when $\Delta\theta_e$ is larger than 80º. As the droplet moves across the junction, θ_A ($\theta_A < 90º$) is lower than θ_e ($\theta_e > 90º$ on a hydrophobic surface). In order to adjust θ_A, the unbalanced Young stress F_A, acting as the drag force before (positive), decreases dramatically and changes its direction (negative). F_A decreases to zero when θ_A arrives at θ_e, and it becomes the drag force again as θ_A exceeds θ_e with the droplet deformation. Based on the above analysis, we can conclude that the unbalanced Young stress could be a driving or resistance force, which is determined by the critical defect strength $\Delta\theta_e$, and the critical defect strength $\Delta\theta_e$ is between 60º and 80º.

5. Conclusions

In this work, we present a derivation of the phase-field moving contact line model with soluble surfactants through the first law of thermodynamics, related thermodynamical relations and the Onsager's variational principle. The derived thermodynamically consistent model consists of two Cahn–Hilliard–type equations governing the evolution of interface and surfactant concentration, the incompressible Navier–Stokes equations and the GNBC for the MCL. With chemical potentials derived from the free energy functional, we analytically obtain certain equilibrium properties of surfactant adsorption, including equilibrium profiles for phase-field variables, the Langmuir isotherm and the equilibrium equation of state. A classical droplet spread case is used to numerically validate the MCL model and equilibrium properties of surfactant adsorption. The influence of surfactants on the contact line dynamics observed in our simulations is consistent with the results obtained by sharp interface models. Numerical results also demonstrate that the equilibrium contact angle of a contaminated droplet can be approximately predicted by the static contact angle of a clean droplet through a linear relationship. Using the proposed model, we investigate the droplet dynamics with soluble surfactants on a chemically patterned surface. It is observed that droplets will form three typical flow states as a result of different surfactant bulk concentrations and defect strengths, specifically, the coalescence mode, the non-coalescence mode and the detachment mode. In addition, a phase diagram for the three flow states is presented. Finally, we study the unbalanced Young stress acting on triple-phase contact points. The unbalanced Young stress could be a driving or resistance force, which is determined by the critical defect strength.

Acknowledgement

We appreciate all reviewers for their constructive suggestions and comments. Jun Yao and Guangpu Zhu acknowledge that this work is supported by the National Science and Technology Major Project (2016ZX05011-001), the Natural Science Foundation of China (51804325, 51674280 and 51774317) and Shandong Provincial Natural Science Foundation (ZR2019JQ21). The work of Shuyu Sun and Jisheng Kou is supported by the KAUST research fund awarded to the

Computational Transport Phenomena Laboratory through the Grant BAS/1/1351-01-01.

References

Alke, A. & D. Bothe, 2009. 3D numerical modeling of soluble surfactant at fluidic interfaces based on the volume-of-fluid method. *FDMP,* 5(4), 345-72.

Alpak, F., A. Samardžić & F. Frank, 2018. A distributed parallel direct simulator for pore-scale two-phase flow on digital rock images using a finite difference implementation of the phase-field method. *Journal of Petroleum Science and Engineering,* 166, 806-24.

Alpak, F.O., B. Riviere & F. Frank, 2016. A phase-field method for the direct simulation of two-phase flows in pore-scale media using a non-equilibrium wetting boundary condition. *Computational Geosciences,* 20(5), 881-908.

Aniszewski, W., T. Arrufat, M. Crialesi-Esposito, S. Dabiri, D. Fuster, Y. Ling, J. Lu, L. Malan, S. Pal & R. Scardovelli, 2019. PArallel, Robust, Interface Simulator (PARIS).

Blake, T.D., J.-C. Fernandez-Toledano, G. Doyen & J. De Coninck, 2015. Forced wetting and hydrodynamic assist. *Physics of Fluids,* 27(11), 112101.

Booty, M. & M. Siegel, 2010. A hybrid numerical method for interfacial fluid flow with soluble surfactant. *Journal of Computational Physics,* 229(10), 3864-83.

Cai, X., H. Marschall, M. Wörner & O. Deutschmann, 2014. A phase field method with adaptive mesh refinement for numerical simulation of 3D wetting processes with OpenFOAM®, in *2nd International Symposium on Multiscale Multiphase Process Engineering (MMPE), Hamburg, Germany*.

Chen, H., S. Sun & T. Zhang, 2017. Energy Stability Analysis of Some Fully Discrete Numerical Schemes for Incompressible Navier–Stokes Equations on Staggered Grids. *Journal of Scientific Computing*, 1-30.

Chen, J., S. Sun & X.-P. Wang, 2014. A numerical method for a model of two-phase flow in a coupled free flow and porous media system. *Journal of Computational Physics,* 268, 1-16.

Copetti, M. & C.M. Elliott, 1992. Numerical analysis of the Cahn-Hilliard equation with a logarithmic free energy. *Numerische Mathematik,* 63(1), 39-65.

Cuenot, B., J. Magnaudet & B. Spennato, 1997. The effects of slightly soluble surfactants on the flow around a spherical bubble. *Journal of Fluid Mechanics,* 339, 25-53.

Ding, H. & P.D. Spelt, 2007. Wetting condition in diffuse interface simulations of contact line motion. *Physical Review E,* 75(4), 046708.

Dupuis, A. & J. Yeomans, 2005. Modeling droplets on superhydrophobic surfaces: equilibrium states and transitions. *Langmuir,* 21(6), 2624-9.

Engblom, S., M. Do-Quang, G. Amberg & A.-K. Tornberg, 2013. On diffuse interface modeling and simulation of surfactants in two-phase fluid flow. *Communications in Computational Physics,* 14(4), 879-915.

Fan, W., H. Sun, J. Yao, D. Fan & Y. Yang, 2019. Homogenization approach for liquid flow within shale system considering slip effect. *Journal of Cleaner Production,* 235, 146-57.

Frank, F., C. Liu, F.O. Alpak, S. Berg & B. Riviere, 2018. Direct numerical simulation of flow on pore-scale images using the phase-field method. *SPE Journal*.

Gao, M. & X.-P. Wang, 2012. A gradient stable scheme for a phase field model for the moving contact line problem. *Journal of Computational Physics,* 231(4), 1372-86.

Gao, M. & X.-P. Wang, 2014. An efficient scheme for a phase field model for the moving contact line

problem with variable density and viscosity. *Journal of Computational Physics,* 272, 704-18.
Garcke, H., K.F. Lam & B. Stinner, 2013. Diffuse interface modelling of soluble surfactants in two-phase flow. *arXiv preprint arXiv:1303.2559*.
Guermond, J.-L. & A. Salgado, 2009. A splitting method for incompressible flows with variable density based on a pressure Poisson equation. *Journal of Computational Physics,* 228(8), 2834-46.
Jacqmin, D., 2000. Contact-line dynamics of a diffuse fluid interface. *Journal of Fluid Mechanics,* 402, 57-88.
James, A.J. & J. Lowengrub, 2004. A surfactant-conserving volume-of-fluid method for interfacial flows with insoluble surfactant. *Journal of Computational Physics,* 201(2), 685-722.
Khatri, S. & A.-K. Tornberg, 2014. An embedded boundary method for soluble surfactants with interface tracking for two-phase flows. *Journal of Computational Physics,* 256, 768-90.
Komura, S. & H. Kodama, 1997. Two-order-parameter model for an oil-water-surfactant system. *Physical Review E,* 55(2), 1722.
Kou, J. & S. Sun, 2018a. Thermodynamically consistent modeling and simulation of multi-component two-phase flow with partial miscibility. *Computer Methods in Applied Mechanics and Engineering,* 331, 623-49.
Kou, J. & S. Sun, 2018b. Thermodynamically consistent simulation of nonisothermal diffuse-interface two-phase flow with Peng–Robinson equation of state. *Journal of Computational Physics,* 371, 581-605.
Kou, J., S. Sun & X. Wang, 2018. Linearly Decoupled Energy-Stable Numerical Methods for Multicomponent Two-Phase Compressible Flow. *SIAM Journal on Numerical Analysis,* 56(6), 3219-48.
Lai, M.-C., Y.-H. Tseng & H. Huang, 2010. Numerical simulation of moving contact lines with surfactant by immersed boundary method. *Communications in Computational Physics,* 8(4), 735.
Laradji, M., H. Guo, M. Grant & M.J. Zuckermann, 1992. The effect of surfactants on the dynamics of phase separation. *Journal of Physics: Condensed Matter,* 4(32), 6715.
Li, J., B. Yu, Y. Wang, Y. Tang & H. Wang, 2015. Study on computational efficiency of composite schemes for convection-diffusion equations using single-grid and multigrid methods. *Journal of Thermal Science and Technology,* 10(1), JTST0009-JTST.
Li, Y. & J. Kim, 2012. A comparison study of phase-field models for an immiscible binary mixture with surfactant. *The European Physical Journal B,* 85(10), 340.
Liu, H., Y. Ba, L. Wu, Z. Li, G. Xi & Y. Zhang, 2018. A hybrid lattice Boltzmann and finite difference method for droplet dynamics with insoluble surfactants. *Journal of Fluid Mechanics,* 837, 381-412.
Liu, H. & Y. Zhang, 2010. Phase-field modeling droplet dynamics with soluble surfactants. *Journal of Computational Physics,* 229(24), 9166-87.
Liu, P., X. Yan, J. Yao & S. Sun, 2019. Modeling and analysis of the acidizing process in carbonate rocks using a two-phase thermal-hydrologic-chemical coupled model. *Chemical Engineering Science*.
Malan, L., Y. Ling, R. Scardovelli, A. Llor & S. Zaleski, 2019. Detailed Numerical Simulations of pore competition in idealized micro-spall using the VOF method. *Computers & Fluids*.
Moukalled, F., L. Mangani & M. Darwish, 2016. The finite volume method in computational fluid dynamics. *An Advanced Introduction with OpenFOAM and Matlab*, 3-8.
Muradoglu, M. & G. Tryggvason, 2008. A front-tracking method for computation of interfacial flows with soluble surfactants. *Journal of Computational Physics,* 227(4), 2238-62.

Onsager, L., 1931a. Reciprocal relations in irreversible processes. I. *Physical Review,* 37(4), 405.

Onsager, L., 1931b. Reciprocal relations in irreversible processes. II. *Physical Review,* 38(12), 2265.

Patil, N.D., V.H. Gada, A. Sharma & R. Bhardwaj, 2016. On dual-grid level-set method for contact line modeling during impact of a droplet on hydrophobic and superhydrophobic surfaces. *International Journal of Multiphase Flow,* 81, 54-66.

Pätzold, G. & K. Dawson, 1995. Numerical simulation of phase separation in the presence of surfactants and hydrodynamics. *Physical Review E,* 52(6), 6908.

Qian, T., X.-P. Wang & P. Sheng, 2003. Molecular scale contact line hydrodynamics of immiscible flows. *Physical Review E,* 68(1), 016306.

Qian, T., X.-P. Wang & P. Sheng, 2004. Power-law slip profile of the moving contact line in two-phase immiscible flows. *Physical Review Letters,* 93(9), 094501.

Qian, T., X.-P. Wang & P. Sheng, 2006. A variational approach to moving contact line hydrodynamics. *Journal of Fluid Mechanics,* 564, 333-60.

Raffa, P., A.A. Broekhuis & F. Picchioni, 2016. Polymeric surfactants for enhanced oil recovery: a review. *Journal of Petroleum Science and Engineering,* 145, 723-33.

Shang, X., Z. Luo & B. Bai, 2019. Droplets trapped by a wetting surface with chemical defects in shear flows. *Chemical Engineering Science,* 195, 433-41.

Shen, J., J. Xu & J. Yang, 2018. The scalar auxiliary variable (SAV) approach for gradient flows. *Journal of Computational Physics,* 353, 407-16.

Shen, J. & X. Yang, 2015. Decoupled, energy stable schemes for phase-field models of two-phase incompressible flows. *SIAM Journal on Numerical Analysis,* 53(1), 279-96.

Shen, J., X. Yang & H. Yu, 2015. Efficient energy stable numerical schemes for a phase field moving contact line model. *Journal of Computational Physics,* 284, 617-30.

Snoeijer, J.H. & B. Andreotti, 2013. Moving contact lines: scales, regimes, and dynamical transitions. *Annual Review of Fluid Mechanics,* 45.

Sui, Y., H. Ding & P.D. Spelt, 2014. Numerical simulations of flows with moving contact lines. *Annual Review of Fluid Mechanics,* 46.

Teigen, K.E., P. Song, J. Lowengrub & A. Voigt, 2011. A diffuse-interface method for two-phase flows with soluble surfactants. *Journal of Computational Physics,* 230(2), 375-93.

Titta, A., M. Le Merrer, F. Detcheverry, P. Spelt & A.-L. Biance, 2018. Level-set simulations of a 2D topological rearrangement in a bubble assembly: effects of surfactant properties. *Journal of Fluid Mechanics,* 838, 222-47.

Van der Sman, R. & S. Van der Graaf, 2006. Diffuse interface model of surfactant adsorption onto flat and droplet interfaces. *Rheologica Acta,* 46(1), 3-11.

Wang, X.-P., T. Qian & P. Sheng, 2008. Moving contact line on chemically patterned surfaces. *Journal of Fluid Mechanics,* 605, 59-78.

Wei, B., J. Hou, M.C. Sukop & H. Liu, 2019. Pore scale study of amphiphilic fluids flow using the Lattice Boltzmann model. *International Journal of Heat and Mass Transfer,* 139, 725-35.

Wodlei, F., J. Sebilleau, J. Magnaudet & V. Pimienta, 2018. Marangoni-driven flower-like patterning of an evaporating drop spreading on a liquid substrate. *Nature communications,* 9(1), 820.

Xu, J.-J. & W. Ren, 2014. A level-set method for two-phase flows with moving contact line and insoluble surfactant. *Journal of Computational Physics,* 263, 71-90.

Xu, J.-J., Y. Yang & J. Lowengrub, 2012. A level-set continuum method for two-phase flows with insoluble surfactant. *Journal of Computational Physics,* 231(17), 5897-909.

Xu, X., Y. Di & H. Yu, 2018. Sharp-interface limits of a phase-field model with a generalized Navier slip boundary condition for moving contact lines. *Journal of Fluid Mechanics,* 849, 805-33.

Yan, X., Z. Huang, J. Yao, Z. Zhang, P. Liu, Y. Li & D. Fan, 2019. Numerical simulation of hydro-mechanical coupling in fractured vuggy porous media using the equivalent continuum model and embedded discrete fracture model. *Advances in Water Resources,* 126, 137-54.

Yang, X., 2017. Numerical Approximations for the Cahn–Hilliard Phase Field Model of the Binary Fluid-Surfactant System. *Journal of Scientific Computing*, 1-21.

Yang, X. & L. Ju, 2017. Efficient linear schemes with unconditional energy stability for the phase field elastic bending energy model. *Computer Methods in Applied Mechanics and Engineering,* 315, 691-712.

Yang, X., J. Zhao, Q. Wang & J. Shen, 2017. Numerical approximations for a three-component Cahn–Hilliard phase-field model based on the invariant energy quadratization method. *Mathematical Models and Methods in Applied Sciences,* 27(11), 1993-2030.

Yu, H. & X. Yang, 2017. Numerical approximations for a phase-field moving contact line model with variable densities and viscosities. *Journal of Computational Physics,* 334, 665-86.

Yue, P., J.J. Feng, C. Liu & J. Shen, 2004. A diffuse-interface method for simulating two-phase flows of complex fluids. *Journal of Fluid Mechanics,* 515, 293-317.

Yun, A., Y. Li & J. Kim, 2014. A new phase-field model for a water–oil-surfactant system. *Applied Mathematics and Computation,* 229, 422-32.

Zampogna, G.A., J. Magnaudet & A. Bottaro, 2019. Generalized slip condition over rough surfaces. *Journal of Fluid Mechanics,* 858, 407-36.

Zeng, Q.-D., J. Yao & J. Shao, 2019. Study of hydraulic fracturing in an anisotropic poroelastic medium via a hybrid EDFM-XFEM approach. *Computers and Geotechnics,* 105, 51-68.

Zhang, J., D.M. Eckmann & P.S. Ayyaswamy, 2006. A front tracking method for a deformable intravascular bubble in a tube with soluble surfactant transport. *Journal of Computational Physics,* 214(1), 366-96.

Zhang, L., Q. Kang, J. Yao, Y. Gao, Z. Sun, H. Liu & A.J. Valocchi, 2015. Pore scale simulation of liquid and gas two-phase flow based on digital core technology. *Science China Technological Sciences,* 58(8), 1375-84.

Zhang, Z., S. Xu & W. Ren, 2014. Derivation of a continuum model and the energy law for moving contact lines with insoluble surfactants. *Physics of Fluids,* 26(6), 062103.

Zhao, J., Q. Kang, J. Yao, H. Viswanathan, R. Pawar, L. Zhang & H. Sun, 2018. The Effect of Wettability Heterogeneity on Relative Permeability of Two‐Phase Flow in Porous Media: A Lattice Boltzmann Study. *Water Resources Research,* 54(2), 1295-311.

Zhu, G., H. Chen, J. Yao & S. Sun, 2019a. Efficient energy-stable schemes for the hydrodynamics coupled phase-field model. *Applied Mathematical Modelling,* 70, 82-108.

Zhu, G., J. Kou, S. Sun, J. Yao & A. Li, 2018. Decoupled, energy stable schemes for a phase-field surfactant model. *Computer Physics Communications,* 233, 67-77.

Zhu, G., J. Kou, S. Sun, J. Yao & A. Li, 2019b. Numerical Approximation of a Phase-Field Surfactant Model with Fluid Flow. *Journal of Scientific Computing*, 1-25.